

An ALOX12–12-HETE–GPR31 signaling axis is a key mediator of hepatic ischemia–reperfusion injury

Xiao-Jing Zhang^{1–4,12}, Xu Cheng^{4,12}, Zhen-Zhen Yan^{5,12}, Jing Fang^{6,12}, Xiaozhan Wang^{1,2}, Weijun Wang⁷, Zhen-Yu Liu^{2,5}, Li-Jun Shen^{1,2}, Peng Zhang^{2–4,8}, Pi-Xiao Wang^{1–4}, Rufang Liao⁹, Yan-Xiao Ji^{2–4,8}, Jun-Yong Wang^{2,4}, Song Tian^{1,2}, Xue-Yong Zhu^{1,2}, Yan Zhang^{1,2}, Rui-Feng Tian^{1,2}, Lin Wang¹⁰, Xin-Liang Ma¹¹, Zan Huang⁵ , Zhi-Gang She^{1–4} & Hongliang Li^{1–4,8}

Hepatic ischemia–reperfusion (IR) injury is a common clinical issue lacking effective therapy and validated pharmacological targets. Here, using integrative ‘omics’ analysis, we identified an arachidonate 12-lipoxygenase (ALOX12)–12-hydroxyeicosatetraenoic acid (12-HETE)–G-protein-coupled receptor 31 (GPR31) signaling axis as a key determinant of the hepatic IR process. We found that ALOX12 was markedly upregulated in hepatocytes during ischemia to promote 12-HETE accumulation and that 12-HETE then directly binds to GPR31, triggering an inflammatory response that exacerbates liver damage. Notably, blocking 12-HETE production inhibits IR-induced liver dysfunction, inflammation and cell death in mice and pigs. Furthermore, we established a nonhuman primate hepatic IR model that closely recapitulates clinical liver dysfunction following liver resection. Most strikingly, blocking 12-HETE accumulation effectively attenuated all pathologies of hepatic IR in this model. Collectively, this study has revealed previously uncharacterized metabolic reprogramming involving an ALOX12–12-HETE–GPR31 axis that functionally determines hepatic IR procession. We have also provided proof of concept that blocking 12-HETE production is a promising strategy for preventing and treating IR-induced liver damage.

IR is an unavoidable consequence of liver surgeries, such as liver transplantation and resection, as well as an occurrence during hemorrhagic shock^{1,2}. IR-related tissue injury accounts for up to 10% of early graft failure and represents a major cause for increased risk of organ rejection and liver dysfunction³. Unfortunately, there are no approved pharmacological interventions for the treatment of hepatic IR injury. Ischemic preconditioning is the only promising strategy to improve outcome⁴; however, the beneficial effects of preconditioning are limited to only a subset of young patients—those who had a long duration of inflow occlusion but a low volume of liver resection⁵. Thus, effective pharmacological treatments for patients with IR-induced liver damage are urgently needed.

The current pathogenic paradigm for hepatic IR injury involves a biphasic process of ischemia-induced cell damage and reperfusion-induced inflammatory response. This concept has led to intense efforts to develop agents with direct anti-inflammatory and antiapoptotic properties, although to date the achieved benefits are unsatisfactory in the clinic^{1,6–8}. Thus, a deeper understanding of the fundamental mechanisms underlying this pathogenic process is required. To achieve this insight, we used an unbiased systemic

investigative approach employing integrative omics analyses. In doing so, we identified a pronounced reprogramming of the lipid metabolic profile in the livers of mice that experienced hepatic IR injury during the ischemic stage as compared to that of mice that underwent IR surgery without vasculature occlusion (sham group). In particular, we found that ALOX12 and its metabolite 12-HETE in the arachidonic acid (AA) metabolic pathway were most greatly enriched in liver at the ischemia stage.

ALOX12 is highly expressed in platelets and is extensively expressed in various cell types, including hepatocytes⁹. Previous studies of ALOX12 mainly focused on its participation in atherosclerosis, thrombosis and cancer because of its capacity to regulate platelet aggregation, cell migration and cancer cell proliferation^{10,11}. However, the role of ALOX12 in hepatic IR injury is unknown. We found that ALOX12–12-HETE signaling markedly promoted IR-induced liver damage via induction of a robust inflammatory response in a GPR31-dependent manner. Notably, blocking 12-HETE production through genetic or pharmacological means substantially ameliorated IR injury across different species, including mouse, pig and *Macaca mulatta* (rhesus macaque). Collectively, our data reveal that lipid metabolic

¹Department of Cardiology, Renmin Hospital of Wuhan University, Wuhan, China. ²Institute of Model Animals of Wuhan University, Wuhan, China. ³Basic Medical School, Wuhan University, Wuhan, China. ⁴Medical Research Institute, School of Medicine, Wuhan University, Wuhan, China. ⁵College of Life Sciences, Wuhan University, Wuhan, China. ⁶Division of Cardiothoracic and Vascular Surgery, Key Laboratory of Organ Transplantation, Ministry of Education and Key Laboratory of Organ Transplantation, Ministry of Health, Tongji Hospital, Tongji Medical College, Huazhong University of Science and Technology, Wuhan, China. ⁷Division of Gastroenterology, Union Hospital, Tongji Medical College, Huazhong University of Science and Technology, Wuhan, China. ⁸Medical Science Research Center, Zhongnan Hospital of Wuhan University, Wuhan, China. ⁹Department of Radiology, Zhongnan Hospital of Wuhan University, Wuhan, China. ¹⁰Department of Hepatic Surgery, Xijing Hospital, Fourth Military Medical University, Xi'an, China. ¹¹Department of Emergency Medicine, Thomas Jefferson University, Philadelphia, Pennsylvania, USA. ¹²These authors contributed equally to this work. Correspondence should be addressed to H.L. (lihl@whu.edu.cn).

Received 19 September; accepted 1 November; published online 11 December 2017; doi:10.1038/nm.4451

reprogramming involving the ALOX12–12-HETE axis determines hepatic IR progression, a previously unappreciated concept, and highlight potential clinical translation of this axis as an early therapeutic interventional target to treat IR-induced liver damage.

RESULTS

Upregulation of ALOX12 in the ischemic stage

Hepatic IR injury is a highly dynamic process and develops rapidly^{12,13}. To gain better insight into the full spectrum of pathological alterations initiated by hepatic IR at the molecular level, we performed digital gene expression (DGE) and proteomics analyses on liver tissue samples obtained from mice after 60 min of ischemia followed by reperfusion for different durations (Fig. 1a). Using these mouse liver DGE data, we performed unsupervised hierarchical clustering and *t*-distributed stochastic neighbor embedding analyses, and we found that samples from six subgroups were clearly separated during the hepatic IR process in a time-dependent manner (Supplementary Fig. 1a,b). The transcriptome reprogramming during IR was visualized by *k*-means clustering analysis, in which the expression trends most related to one another were categorized into six clusters (Fig. 1b). Notably, ischemia without reperfusion elicited a highly unique gene expression profile, in which genes involved in lipid metabolism were identified as dramatically changed in comparison to the sham group (Fig. 1b and Supplementary Fig. 1c). In contrast, selective enrichment of genes and pathways involved in inflammatory signal transduction, immune response, cell death and DNA repair were observed during reperfusion, particularly at 6, 12 and 24 h after reperfusion (Fig. 1b and Supplementary Fig. 1c). These multivariate analyses indicate that robust transcriptome reprogramming in response to hepatic IR injury occurs as early as the ischemic stage, with lipid metabolic reprogramming among the features most substantially changed at that stage.

Deeper analysis of the most differentially expressed genes during the ischemic stage further highlighted AA metabolism as the most changed pathway on the basis of the number of changed genes and statistical significance (Fig. 1c and Supplementary Fig. 1d). Notably, the AA pathway also stood out in the proteomics data set with a high correlation with the DGE data (Fig. 1d). Among the factors involved in the AA pathway, *Alox12*, encoding a lipoxygenase that targets the conversion of AA to 12-HETE^{14,15}, was the most upregulated gene at the mRNA level, as determined by analysis of differentially expressed gene, and *Alox12* was one of the three most upregulated proteins in our proteomics data set (Fig. 1e and Supplementary Fig. 1e). This dramatic increase of ALOX12 expression was confirmed by qPCR and immunoblotting, and there was no such alteration in the mRNA or protein expression of two other ALOX family members (ALOX5 and ALOX15) during ischemia in comparison to the sham group (Supplementary Fig. 1f,g). The induction of ALOX12 expression was sustained throughout the entire process of hepatic IR injury, with maximal *Alox12* mRNA expression at 6 h after reperfusion (Fig. 1f).

To explore the human relevance of these findings, we measured ALOX12 mRNA expression in liver tissues from individuals with hepatic IR due to liver resection and compared expression in these samples with that in tissue from the same individual at baseline (i.e., before exposure to ischemia). We found significantly greater ALOX12 mRNA expression in the ischemia and reperfusion stages as compared to baseline (Fig. 1g). In line with the increased mRNA expression, the ALOX12 protein level was also much higher at the ischemic and reperfusion phases than at baseline in both the mouse hepatic IR model and the human subjects who underwent liver resection (Fig. 1h–k and Supplementary Fig. 1h).

12-HETE is the primary metabolite affected by changes in ALOX12 expression during ischemia–reperfusion

As noted above, ALOX12 is a lipoxygenase with specific activity for conversion of AA to 12-HETE (Supplementary Fig. 2a). Among the major AA metabolites whose formation is catalyzed by lipoxygenases or cytochrome P450 enzymes, 12-HETE showed the most markedly increased content in both the hepatic tissue and serum of mice after hepatic IR insult, whereas the levels of other HETEs, e.g., 5-, 15- and 20-HETE, were not as robustly increased (Fig. 2a and Supplementary Fig. 2b,c). Indeed, 12-HETE was the most dramatically and earliest changed species among the tested AA metabolites (Fig. 2a and Supplementary Fig. 2b,c). Furthermore, the increase in 12-HETE was temporally in sync with the upregulation of ALOX12 in both ischemic livers and primary hepatocytes challenged by hypoxia (Fig. 2b,c). In cultured primary hepatocytes, hypoxia induced a dramatic increase in ALOX12 protein expression (Fig. 2d,e). When we genetically knocked down *Alox12* via short hairpin RNA (shRNA), 12-HETE production was greatly inhibited, whereas *Alox12* overexpression increased 12-HETE content in cell lysates as compared to control cells (Fig. 2f–g).

To obtain more evidence supporting the role of ALOX12 in 12-HETE accumulation during hepatic IR injury, *Alox12*-knockout (*Alox12*-KO) mice and mice with hepatocyte-specific expression of an *Alox12* transgene (*Alox12*-HTG) were generated (Supplementary Fig. 2d,e). In accordance with the data obtained *in vitro*, ALOX12 deficiency *in vivo* correlated with significantly lower 12-HETE content in both liver and serum as compared to wild-type (WT) control mice, whereas *Alox12*-HTG mice exhibited greater 12-HETE content in liver and serum relative to the corresponding nontransgenic (NTG) controls (Fig. 2h,i). Finally, we found that 12-HETE production and secretion were significantly greater during IR when compared to baseline in individuals subjected to hepatic IR surgery during liver resection (Fig. 2j).

Manipulation of *Alox12* expression affects the degree of ischemia–reperfusion-induced liver injury

To obtain direct evidence supporting a causative role for changes in the ALOX12–12-HETE axis in hepatic IR injury, we subjected *Alox12*-KO mice to a 60-min liver ischemia followed by 6-h reperfusion. Serum aminotransferase levels were significantly decreased in *Alox12*-KO mice subjected to hepatic IR as compared to WT controls (Fig. 3a). In accordance with this finding, IR-induced tissue necrosis and cell death were greatly ameliorated in the liver by *Alox12* knockout, as evidenced by marked differences in both morphological staining and the expression of apoptotic regulators (Fig. 3b–d). Moreover, *Alox12* deficiency significantly lowered the serum concentrations of inflammatory cytokines and chemokines (Fig. 3e). This effect was accompanied by lower expression levels of genes encoding inflammatory mediators, as well as by less inflammatory cell infiltration into the livers of *Alox12*-KO mice at 6 h after reperfusion (Fig. 3f,g). In accordance with these differences, activation of NF-κB signaling was blunted in the livers of *Alox12*-KO mice as compared to WT controls at 6 h after reperfusion (Fig. 3h).

In contrast with *Alox12* deficiency, the hepatocyte-specific overexpression of *Alox12* elicited a remarkable exacerbation of liver dysfunction, cell death and inflammatory response as compared to NTG controls in response to hepatic IR surgery (Supplementary Fig. 3). It should be noted that no significant difference relative to control mice in serum levels of liver enzymes, tissue necrosis, inflammatory marker expression or NF-κB signaling was observed in *Alox12*-KO mice or mice

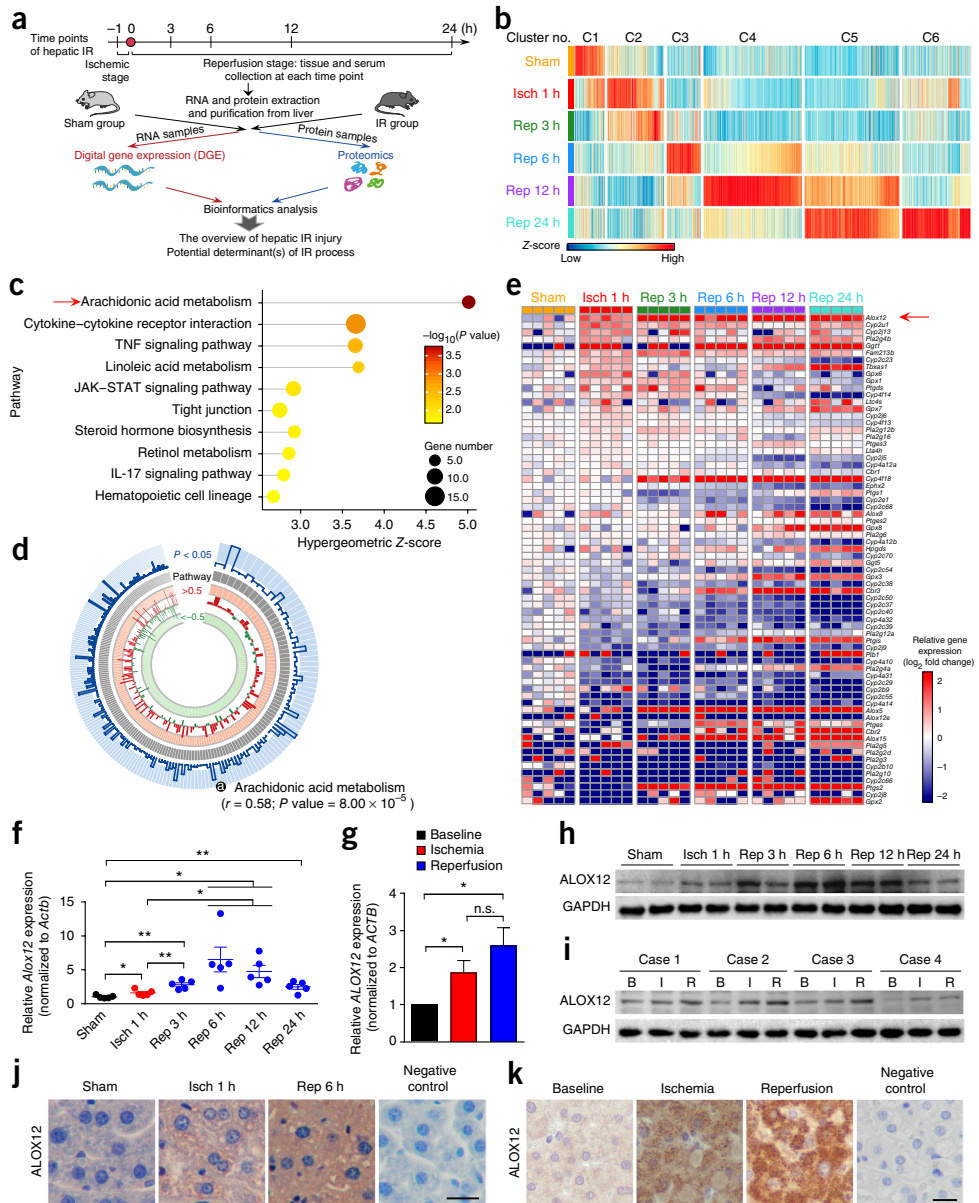


Figure 1 ALOX12 is dramatically upregulated during hepatic IR injury. **(a)** Schematic of the experimental strategy used to identify the potential determinants of hepatic IR injury. Mice without blood blockage served as controls (sham group). **(b)** Six k-means clusters showing distinct and specific expression trends for each period of hepatic IR injury determined by the normalized average gene expression level of biological replicates ($n = 5$ mice in each period of hepatic IR injury) using the Z-score transformation method. **(c)** Kyoto Encyclopedia of Genes and Genomes (KEGG) pathway enrichment analysis of the identified differentially expressed genes between ischemia and sham groups. The ten most significantly enriched pathways ($P < 0.05$ by Fisher's exact test) are shown. **(d)** Circos plot showing the correlations between the proteomics and DGE data. Histograms with a blue border at the outer edge of the circle represent correlations with a $-\log_{10}P$ value, and only correlations with $P < 0.05$ (by correlation analysis with Pearson correlation coefficient) extend to the light blue area. Correlation tracks are shown inside the circular layout as follows: red bars represent positive correlation ($r > 0$), and bars located in the light red area indicate r values larger than 0.50; green bars represent negative correlations, and the light green area indicates an r value lower than -0.50 by correlation analysis with Pearson correlation coefficient. **(e)** Heat maps generated using the mRNA expression of members in the AA metabolism pathway detected by the DGE. In **a-e**, $n = 5$ mice in each group for DGE; $n = 15$ mice in each group with samples from 5 mice pooled for proteomics analysis; $n = 3$ pools in each group for proteomics analysis. **(f)** Relative *Alox12* mRNA expression levels (normalized to that of β -actin-encoding gene *Actb*) in the livers of mice at 1 h after ischemia (isch) or at 3, 6, 12 and 24 h after reperfusion (rep). $n = 5$ mice in each group. **(g)** The relative mRNA expression of *ALOX12* (normalized to that of *ACTB*) in the livers of individuals subjected to hepatic IR surgery due to liver resection. $n = 19$ individuals in each group. **(h)** *ALOX12* protein expression levels in the livers of mice subjected to 60-min ischemia followed by reperfusion for the indicated periods. $n = 6$ mice in each group; $n = 3$ western blots for each band. **(i)** Representative western blot (of $n = 5$ western blots) showing *ALOX12* protein expression in the livers of individuals subjected to hepatic IR surgery. B, baseline; I, ischemia; R, reperfusion. GAPDH served as a loading control. $n = 19$ individuals in each group. **(j)** Representative images of immunohistological staining showing *ALOX12* expression profiles in the livers of mice after hepatic ischemia for 60 min or at 6 h after reperfusion. $n = 4$ mice for each group with 24 images for each mouse. Scale bar, 20 μ m. **(k)** Representative images of *ALOX12* expression profiles in the liver sections of individuals subjected to hepatic IR surgery ($n = 6$ subjects in each group with 24 images for each subject). Scale bar, 20 μ m. For statistical analysis, a two-tailed Student's *t*-test (**f**) or one-way ANOVA with Tamhane's T2 (M) *post hoc* analysis (**g**) was used. * $P < 0.05$, ** $P < 0.01$. n.s., not significant. In all statistical plots, data are shown as the mean \pm s.e.m.

with *Alox12* overexpression at the baseline condition, which is consistent with a previous report¹⁶ (Fig. 3 and Supplementary Fig. 3).

12-HETE promotes hepatic ischemia–reperfusion injury via induction of a burst of inflammation

We next explored the underlying mechanisms responsible for the pathological effect of ALOX12–12-HETE signaling on hepatic IR by

determining the transcriptome data set of livers from mice subjected to the hepatic IR surgery shown in Figure 1a. Using weighted gene coexpression network analysis (WGCNA) to identify pairwise correlation between genes across all samples, we identified numerous gene modules with a high degree of coordinated expression and labeled these modules with different colors. We then established the overall degrees of correlation of genes in the modules with expression of *Alox12* or

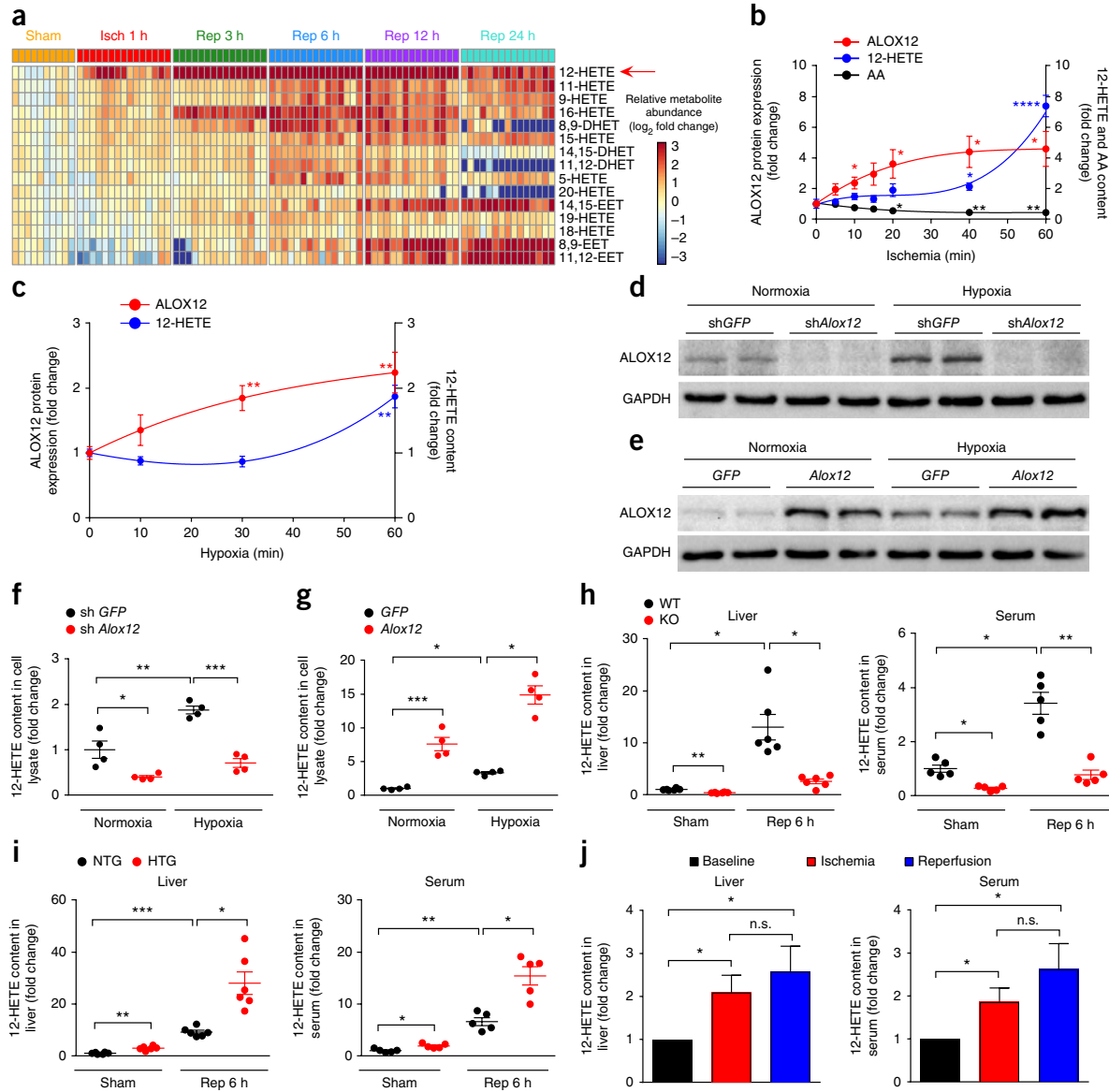


Figure 2 ALOX12 directly promotes 12-HETE accumulation in hepatic IR injury. **(a)** Heat map showing the contents of major AA metabolites catalyzed by lipoxygenases or cytochrome P450 enzymes in the livers of mice at the indicated time points during the hepatic IR process. $n = 10$ mice in the sham group, $n = 15$ mice in other groups. **(b)** Time-dependent changes in the profiles of relative ALOX12 protein expression, 12-HETE content and AA content in the livers of mice at indicated time points after hepatic ischemia ($n = 6$ mice in each time point). **(c)** Relative protein expression level of ALOX12 and 12-HETE content in the cell lysates of primary hepatocytes after 10, 30 and 60 min of hypoxia. $n = 3$ independent experiments. For **b** and **c**, data are shown as the mean \pm s.e.m. * $P < 0.05$, ** $P < 0.01$, *** $P < 0.0001$ compared to ischemia at 0 min (**b**) or hypoxia at 0 min (**c**) by two-tailed Student's *t*-test. **(d,e)** Representative western blot (of two western blots for each band) showing ALOX12 protein expression in cell lysates of primary hepatocytes following *Alox12* knockdown (**d**) or *Alox12* overexpression (**e**) by adenovirus under the condition of normoxia or hypoxia for 1 h. **(f,g)** 12-HETE content in the cell lysates of primary hepatocytes treated as in **d** and **e**. For **d–g**, $n = 4$ independent experiments. **(h)** 12-HETE content in the livers (left) and serum (right) of *Alox12*-KO and WT controls at 6 h after reperfusion or in the sham group. **(i)** 12-HETE content in the livers (left) and serum (right) of *Alox12*-HTG and NTG control mice in the sham and 6-h reperfusion groups. In **h** and **i**, $n = 5$ mice in each group for detection of serum 12-HETE; $n = 5$ mice in sham groups for liver 12-HETE examination; $n = 6$ mice in rep 6 h groups for liver 12-HETE examination. **(j)** 12-HETE content in the livers (left; $n = 17$) and serum (right; $n = 19$) of human individuals subjected to hepatic IR injury. For statistical analysis in **f–j**, one-way ANOVA with Tamhane's T2 (M) post hoc analysis was used. * $P < 0.05$, ** $P < 0.01$, *** $P < 0.0001$. In all statistical plots, data are shown as mean \pm s.e.m.

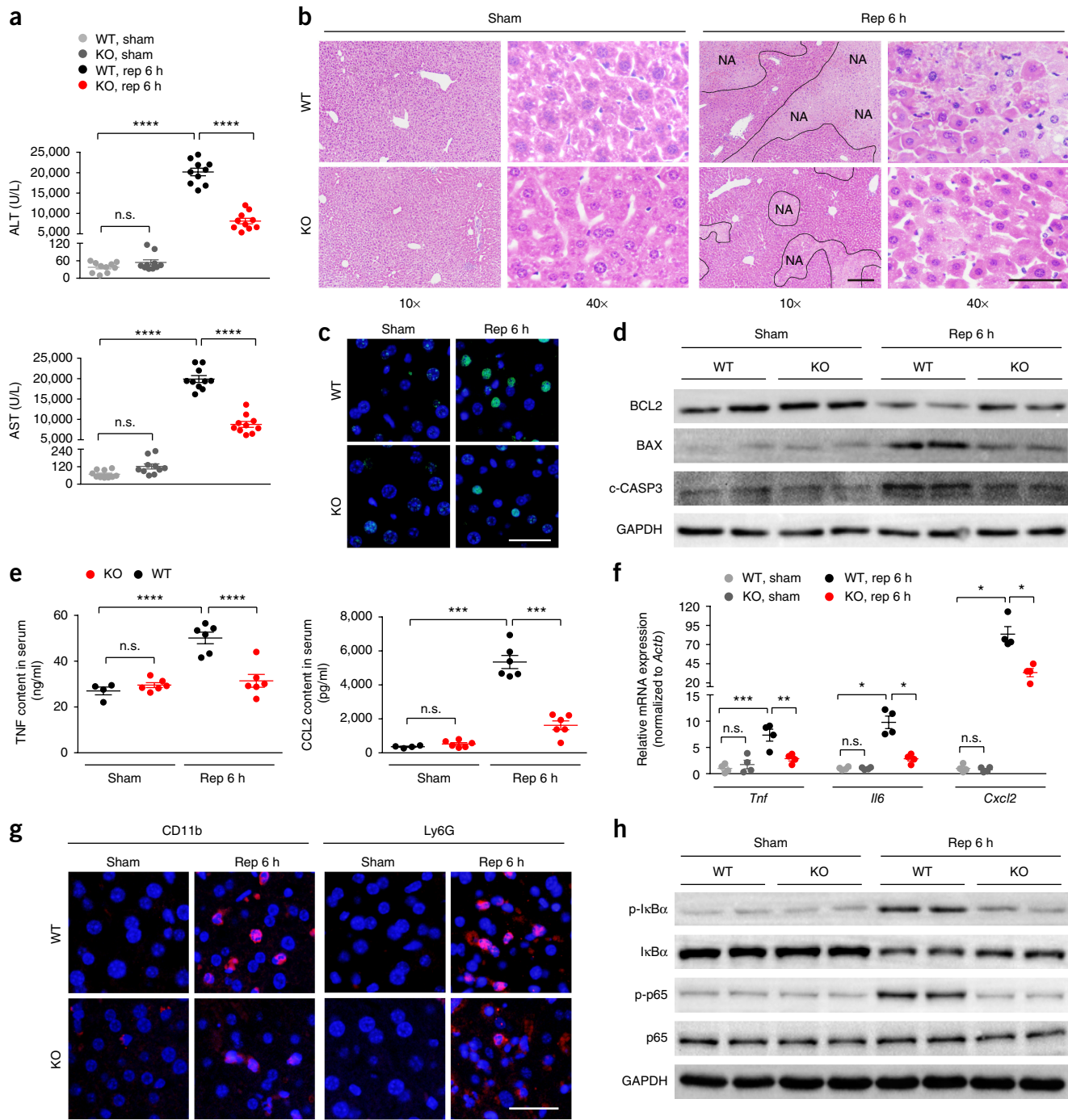


Figure 3 *Alox12* knockout inhibits IR-induced liver dysfunction, cell death and inflammation. **(a)** ALT and AST levels in the serum of *Alox12*-deficient mice (KO) or WT controls in the sham group (at baseline) or at 6 h after reperfusion. *n* = 10 mice in each group. **(b,c)** H&E (**b**) and terminal deoxynucleotidyl transferase dUTP nick-end labeling (TUNEL) (**c**) staining of liver sections from WT mice and *Alox12*-KO mice in the sham group or at 6 h after reperfusion. *n* = 4 mice per group at each time point with 24 images for each mouse. Scale bar, 200 μ m for H&E staining (10 \times); 50 μ m for H&E staining (40 \times); 20 μ m for TUNEL images. NA, necrotic area. **(d)** Representative western blot (*n* = 3 western blots) showing protein expression of BCL2, BAX and cleaved caspase-3 (c-CASP3) in the livers of mice in the indicated groups. *n* = 6 mice for each group. **(e)** Tumor necrosis factor (TNF) and CCL2 content in the serum of WT mice and *Alox12*-KO mice in the sham group and at 6 h after reperfusion. *n* = 4 mice in sham WT group and *n* = 6 mice in other groups. **(f)** The relative mRNA expression levels of cytokines and chemokines in the livers of WT mice and *Alox12*-KO mice before and at 6 h after hepatic IR injury. Gene expression was normalized to the expression of *Actb*. *n* = 4 mice per group. **(g)** Representative images of immunofluorescent staining of CD11b⁺ (left) and Ly6G⁺ (right) inflammatory cells (red) in liver sections from mice in the indicated groups. The nuclei were labeled with DAPI (blue). *n* = 4 mice in each group with 24 images for each mouse. Scale bar, 20 μ m. **(h)** Activation of NF- κ B signaling in the livers of WT mice and *Alox12*-KO mice in the sham group and at 6 h after reperfusion. p-, phosphorylated. GAPDH served as a loading control. *n* = 6 mice for each group; *n* = 3 western blots for each band. For statistical analysis, one-way ANOVA with Bonferroni's *post hoc* analysis (for TNF in **e** and *Tnf* in **f**) or with Tamhane's T2 (M) *post hoc* analysis (for **a**, CCL2 in **e** and *Il6* and *Cxcl2* in **f**) was used. **P* < 0.05, ***P* < 0.01, ****P* < 0.001, *****P* < 0.0001. In all statistical plots, data are shown as the mean \pm s.e.m.

12-HETE levels. Specifically, the yellow module showed the highest degree of positive correlation with *Alox12* expression and 12-HETE levels, and members of the yellow module were significantly enriched in multiple inflammatory signaling pathways and for genes encoding inflammatory mediators (Fig. 4a,b). Examination of the temporal profile showed that the elevated 12-HETE production occurred before or concomitantly with the upregulation of proinflammatory mediators (Supplementary Fig. 4a,b), suggesting a potential role for 12-HETE in inflammatory regulation during hepatic IR.

Supporting this conclusion, we observed significantly increased phosphorylation of the NF-κB subunit p65 and MAPK subunits JNK, p38 and ERK, the major downstream mediators of pathways enriched in the yellow cluster, when *Alox12* was overexpressed in primary hepatocytes, which correlated with enhanced expression of representative inflammatory genes (Supplementary Fig. 4c,d). *Alox12* knockdown led to the opposite effect on these readouts in primary hepatocytes upon hypoxia challenge (Supplementary Fig. 4e,f). The exacerbating effect of ALOX12 on the activation of key inflammatory signals was further confirmed in *Alox12*-KO and *Alox12*-HTG mice *in vivo* at 6 h after reperfusion (Supplementary Fig. 4g,h). Moreover, direct treatment of primary hepatocytes with 12-HETE resulted in greater p65, JNK, p38 and ERK phosphorylation and inflammatory gene expression as compared to vehicle treatment (Fig. 4c,d), supporting the notion that the proinflammatory action of ALOX12 is mediated by its primary product, 12-HETE. Blocking 12-HETE production with ML355, a specific ALOX12 inhibitor¹⁷, largely abolished the impact of hypoxic injury on inflammation induction in primary hepatocytes *in vitro* (Fig. 4e–g).

GPR31 is responsible for 12-HETE-mediated hepatic ischemia–reperfusion injury

To gain a better understanding of how 12-HETE promotes inflammation, we performed additional RNA-seq analyses in primary hepatocytes under normoxia or challenge by hypoxia in the presence or absence of 12-HETE. Remarkably, the cellular pathways and genes most affected by 12-HETE (as determined on the basis of fold change) were mostly implicated in inflammation-related processes, as revealed by gene set enrichment analysis (GSEA) and confirmed by qPCR (Fig. 5a and Supplementary Fig. 5a,b). In the context of a gene coexpression network (Fig. 4a), the heaviest 5% weight edges of the highlighted overlapped leading genes that changed in response to 12-HETE under normoxia and hypoxia conditions (Fig. 5a and Supplementary Fig. 5a) were used for gene ontology (GO) analysis to determine enriched terms in 12-HETE-mediated hepatic IR injury (Fig. 5b). Notably, the neighboring genes most connected to the leading genes were clearly enriched for terms related to G-protein-coupled receptor (GPCR) signaling (Fig. 5b).

GPCR-mediated signaling has long been implicated in inflammatory regulation, and GPCRs can serve as receptors for numerous lipid metabolites¹⁸. Among four well-established ‘lipid-sensing’ GPCRs (i.e., free fatty acid receptor 1 (FFAR1)–FFAR4), FFAR1 (also known as GPR40) and FFAR4 (also known as GPR120) are known to be responsive to long-chain fatty acids^{19–21}. Two other GPCRs, GPR31 and GPR75, have also been reported to be receptors for HETEs^{22,23}. Therefore, we screened GPR40, GPR120, GPR31 and GPR75 to identify the receptor isotype responsible for 12-HETE-elicited signaling in response to hepatic IR insult. *GPR31* knockdown in the human L02 hepatocyte cell line abolished 12-HETE-induced activation of protein kinase C (PKC)–JNK signaling, whereas silencing of the other three GPCRs had no detectable impact on 12-HETE function (Fig. 5c). The

effect of *GPR31* inactivation on 12-HETE function was further confirmed by RNA-seq and GSEA analyses (Fig. 5d,e and Supplementary Fig. 5c). Notably, *GPR31* rescue in *GPR31*-deficient L02 cells globally restored the effects of 12-HETE on inflammation-related pathways and genes, as demonstrated by RNA-seq (Fig. 5d,e and Supplementary Fig. 5c) and further confirmed by western blotting and qPCR (Supplementary Fig. 5d,e).

To obtain *in vivo* evidence supporting the role of *GPR31* in ALOX12–12-HETE-mediated liver injury, we next generated global *Gpr31b*-KO mice (*Gpr31b* corresponds to *GPR31* in humans; Supplementary Fig. 5f) and exposed them to hepatic IR surgery. Liver dysfunction, cell death and inflammatory induction were consistently and significantly inhibited by *Gpr31b* ablation as compared to WT controls at 6 h after reperfusion (Fig. 5f–h and Supplementary Fig. 5g,h).

Blocking 12-HETE production inhibits hepatic ischemia–reperfusion injury in mice and pigs

Considering the critical effect of 12-HETE on hepatic IR injury, we examined whether blocking 12-HETE production using two previously reported ALOX12 inhibitors, ML355 and CDC^{17,24,25}, could suppress these pathologies. Both ALOX12 inhibitors were highly effective in inhibiting 12-HETE production and suppressing liver damage after hepatic IR insult, but ML355 exhibited a stronger capacity than CDC (Supplementary Fig. 6a–c). Furthermore, we found that the protective effect of ML355 against liver damage was dose dependent and consistent with the inhibition of 12-HETE production (Supplementary Fig. 6d–f). The protective effects of ML355 lasted over the entire hepatic IR period, as evidenced by the significantly reduced serum aminotransferase levels and lower cell death at each tested time point as compared to the vehicle-treated group (Supplementary Fig. 6g–i). Remarkably, hepatic IR-induced inflammatory responses, including cytokine and chemokine production, inflammatory cell infiltration and signaling transduction, were all attenuated by ML355 treatment (Supplementary Fig. 6j–m).

Although small experimental animals, particularly mice, have made an invaluable contribution to understanding of disease at the molecular level, phenotypic differences between rodents and humans remain a roadblock in developing effective therapies for clinical application. Compared to the mouse, the pig provides a more appropriate preclinical model for disease therapy, especially surgical operation, because of the similarities in size, biology and anatomy between pig and human organs²⁶. In a porcine model of hepatic IR injury (Supplementary Fig. 7a), we observed a reduction in liver and serum 12-HETE production after hepatic IR insult in the ML355-treated group as compared to vehicle-treated controls (Supplementary Fig. 7b). Moreover, ML355 treatment led to a considerable inhibition of liver dysfunction, cell death and inflammatory response at each examined time point (Supplementary Fig. 7c–h).

ML355 inhibits liver damage in a nonhuman primate model of hepatic ischemia–reperfusion

Although the major therapeutic effects of ML355 treatment in both mouse and pig models of hepatic IR injury indicate a conserved underlying mechanism for hepatic IR injury and a promising strategy for treating liver damage induced by IR surgery, demonstration of a potential translation to the clinic still requires use of an animal model that more closely resembles humans. Thus, we established a hepatic IR model in a nonhuman primate, the rhesus macaque, with a range of 30–120 min for the ischemic period. The peak values and time course profiles of serum alanine transaminase (ALT), aspartate

transaminase (AST) and alkaline phosphatase (ALP) observed in individuals subjected to liver resection in the clinic were used as standards (Fig. 6a). Liver damage in the monkeys was further evaluated

by perfusion computed tomography (CT). We found that a 30-min ischemic period was too short to induce substantial hepatic IR injury in the monkeys, whereas a 120-min ischemic period induced a liver

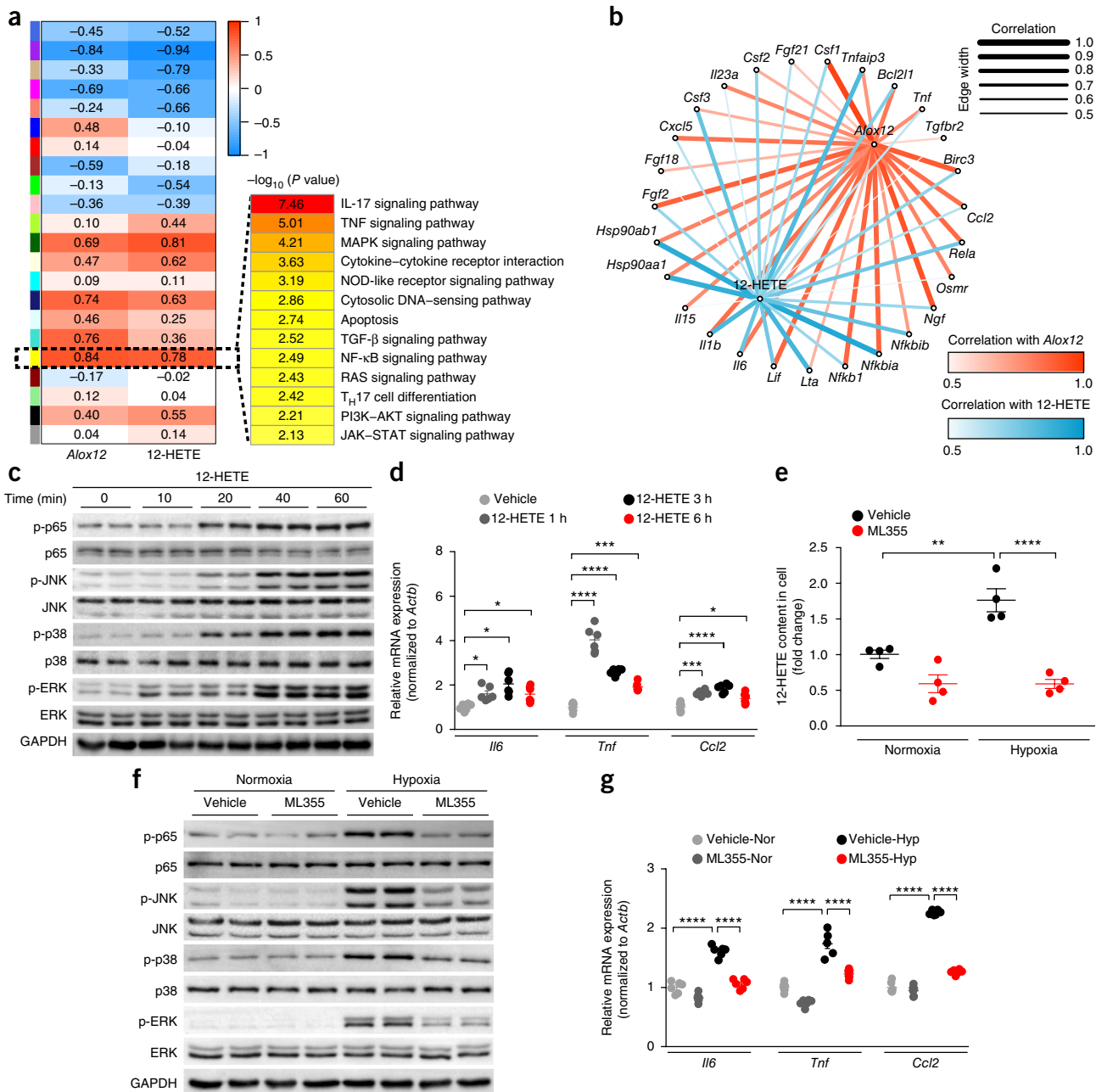


Figure 4 12-HETE promotes hepatic IR injury by inducing a burst of inflammation. **(a)** Left, Pearson correlation coefficient between *Alox12* or 12-HETE and the coexpression modules (represented by the colored boxes at the left of the table) determined based on WGCNA using the DGE data in **Figure 1a** ($n = 6$ groups with 5 mice in each). Right, KEGG analysis results for genes in the yellow coexpression module that were significantly enriched in the indicated inflammatory pathways ($P < 0.05$ by Fisher's exact test). **(b)** Correlations between the expression of *Alox12* or the level of 12-HETE and the expression of core genes related to the pathways listed in **a**. The correlation was visualized in a user-defined manner with line width and color saturation; stronger correlations are indicated by thicker lines and darker colors. **(c,d)** Representative western blots ($n = 3$ western blots for each band) showing phosphorylated and total p65, JNK, p38 and ERK protein expression (**c**) and qPCR results showing relative mRNA expression levels for *Il6*, *Tnf* and *Ccl2* (**d**) in primary hepatocytes treated with 12-HETE for the indicated periods. $n = 3$ independent experiments with 2 replicates each. **(e–g)** 12-HETE content (**e**), phosphorylated and total levels of p65, JNK, p38 and ERK (**f**) and relative mRNA expression of cytokines and chemokines (**g**) in primary hepatocytes treated with ML355 (10 μ M) under normoxia (Nor) or hypoxia (Hyp) conditions. For western blot analysis, GAPDH served as a loading control. In the qPCR assay, mRNA expression of genes was normalized to that of *Actb*. $n = 4$ independent experiments for **e**; $n = 3$ independent experiments with two replicates each for **f** and **g**. For statistical analysis, one-way ANOVA with Bonferroni's *post hoc* analysis (for *Ccl2* in **d** and for **e** and **g**) or with Tamhane's T2 (M) *post hoc* analysis (for *Tnf* and *Il6* in **d**) was used. * $P < 0.05$, ** $P < 0.01$, *** $P < 0.001$, **** $P < 0.0001$. In all statistical plots, data are shown as mean \pm s.e.m.

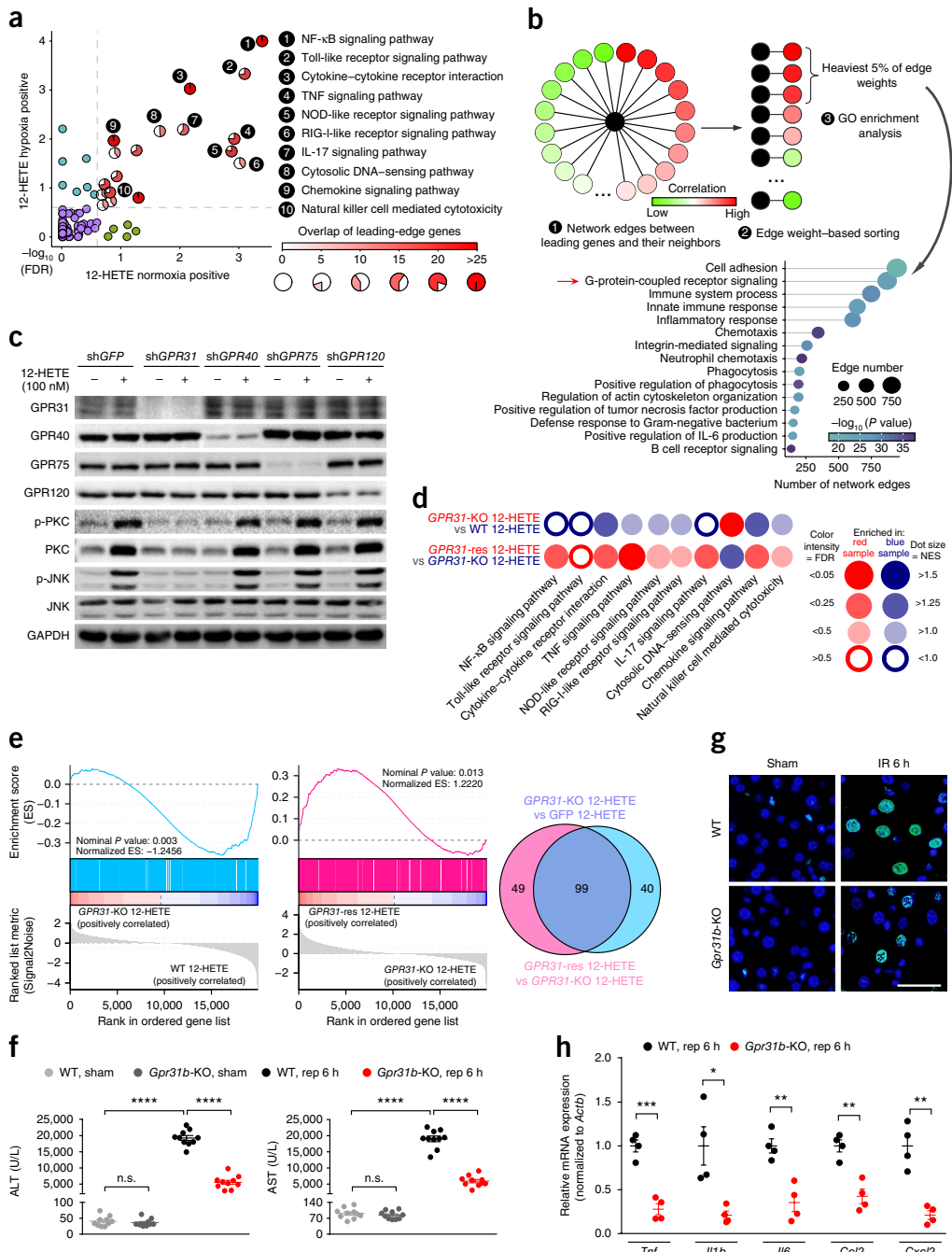


Figure 5 GPR31 is responsible for 12-HETE-mediated hepatic IR injury. **(a)** The major pathways contributing to 12-HETE function determined by GSEA of RNA-seq results from primary hepatocytes treated with 12-HETE (100 nM) under normoxia or hypoxia conditions. The red area in each numbered circle indicates the number of overlapped leading-edge genes (the core genes that account for their gene set's enrichment signal) induced by 12-HETE under normoxia and hypoxia. Analysis included data from four independent experiments. **(b)** Schematic of GO analysis showing that GPCR signaling is a major contributor to 12-HETE function. The data used in this GO analysis were from the leading genes highlighted in the red areas of the circles in the RNA-seq data shown in **a** and **Supplementary Figure 5a** with the heaviest 5% of edge weights ($n = 4$ samples from independent experiments for each group). The 15 most significantly enriched pathways ($P < 0.05$ by Fisher's exact test; edge number > 100) are shown. **(c)** Levels of phosphorylated and total PKC and JNK in *GPR31*-, *GPR40*-, *GPR75*- or *GPR120*-knockdown cells treated with 12-HETE or vehicle control for 1 h. $n = 3$ independent experiments. GAPDH served as a loading control. **(d)** Dot blot representing pairwise GSEA comparison of RNA-seq data among 12-HETE-treated hepatocytes (WT control, *GPR31*-KO and *GPR31*-rescue (*GPR31*-res) groups; $n = 3$ in each group). Dot color indicates that the gene signature set is enriched in the group with corresponding font color. NES, normalized enrichment score. **(e)** Left, GSEA showing the merged gene sets of genes in the pathways shown in **Figure 5d**. Right, Venn diagram showing shared leading genes between two comparisons. Data were statistically analyzed by GSEA based on three independent experiments. **(f)** ALT and AST content in the serum of WT mice and *Gpr31b*-KO mice in the sham group or at 6 h after reperfusion. $n = 10$ mice in each group. **(g)** Representative images of TUNEL staining (green) of liver sections at 6 h after reperfusion of mice with *Gpr31b* knockout or WT controls. The nuclei were labeled with DAPI (blue). $n = 4$ mice for each group with 24 images for each mouse. Scale bar, 20 μ m. **(h)** Relative mRNA expression of inflammatory cytokines and chemokines ($n = 4$ mice in each group) in the livers of mice in the indicated groups. For statistical analysis, one-way ANOVA with Tamhane's T2 (M) post hoc analysis (**f**) or a two-tailed Student's *t*-test (**h**) was used. * $P < 0.05$, ** $P < 0.01$, *** $P < 0.001$, **** $P < 0.0001$. In all statistical plots, data are shown as mean \pm s.e.m.

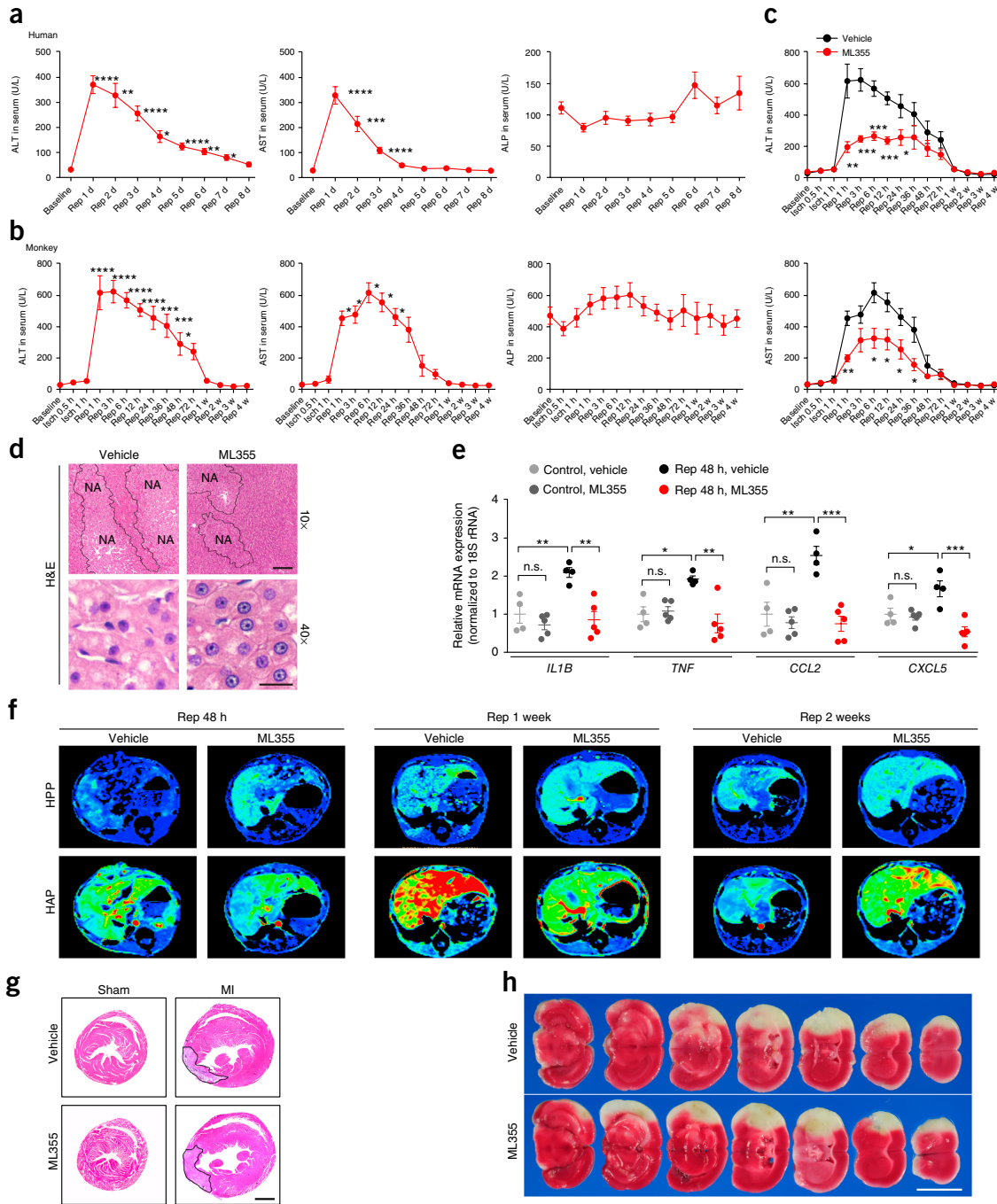


Figure 6 ML355 inhibits liver damage in a monkey hepatic IR model. **(a,b)** Serum ALT, AST and ALP levels of human subjects after liver resection (**a**, $n = 38$ individuals) and of monkeys subjected to 60-min ischemia followed by periods of reperfusion of varying duration (**b**, $n = 5$ in each group). w, weeks. * $P < 0.05$, ** $P < 0.01$, *** $P < 0.001$, **** $P < 0.0001$ compared to the corresponding baselines by one-way ANOVA with Tamhane's T2 (**M**) (**a**) and with Bonferroni's *post hoc* analysis (**b**). **(c)** Serum ALT and AST levels ($n = 5$ in vehicle group, $n = 6$ in ML355 group) in monkeys treated with ML355 (3 mg per kg body weight) or with vehicle after 60 min of hepatic ischemia followed by the indicated periods of reperfusion. * $P < 0.05$, ** $P < 0.01$, *** $P < 0.001$ compared to corresponding time points of vehicle group by two-tailed Student's *t*-test. **(d)** Representative images of H&E staining on monkey liver sections in ML355- and vehicle-treated groups after 48 h of reperfusion. $n = 5$ monkeys per group with 24 images for each monkey. Scale bar, 200 μ m for H&E staining (10x); 20 μ m for H&E staining (40x). **(e)** Relative mRNA expression (normalized to that of 18S rRNA) of inflammatory mediators in the IR-challenged hepatic lobes and control lobes of monkeys in ML355- and vehicle-treated groups at 48 h after reperfusion. $n = 4$ monkeys in the vehicle-treated group and $n = 5$ monkeys in the ML355-treated group. * $P < 0.05$, ** $P < 0.01$, *** $P < 0.001$ by one-way ANOVA with Bonferroni's *post hoc* analysis. **(f)** Representative perfusion CT images of livers from monkeys treated with vehicle or ML355 at 48 h, 1 week and 2 weeks after reperfusion. $n = 5$ monkeys at each time point for each group. Each image was generated from 39 scans in each monkey. HAP, hepatic arterial perfusion; HPP, hepatic portal perfusion. **(g)** Representative images of H&E staining of heart sections from mice treated with ML355 or vehicle control in the sham group or at 7 d after MI surgery. $n = 4$ mice for each group with 2 consecutive sections for each mouse. Scale bar, 1 mm. **(h)** Representative images of 2,3,5-triphenyl-2-H-tetrazolium chloride (TTC) staining of serial brain sections of mice at 24 h after stroke. $n = 8$ mice in each group with 7 consecutive sections for each mouse. Scale bar, 5 mm. In all statistical plots, data are shown as mean \pm s.e.m.

damage response that was too severe to be repaired by 4 weeks following injury (**Supplementary Fig. 8a–c**). Notably, the peak values in the time course profiles of serum levels of ALT, AST and ALP after 60-min ischemia of the left lateral lobe of the liver followed by reperfusion closely matched those observed in human individuals subjected to liver resection (**Fig. 6a,b** and **Supplementary Fig. 8a**). Furthermore, perfusion CT clearly showed that the hepatic portal perfusion was greatly reduced at 48 h after reperfusion following 60-min ischemia and then slightly increased at 1 and 2 weeks after reperfusion, whereas the hepatic arterial perfusion showed a compensatory increase after hepatic IR surgery (**Supplementary Fig. 8d**). At 4 weeks after reperfusion, the CT perfusion parameters of the monkeys were restored to normal levels in the 60-min ischemia model (**Supplementary Fig. 8d**). In short, by using a 60-min ischemia, we developed a monkey model of hepatic IR injury that resembles the disease in the clinical setting.

In this nonhuman primate model, we observed a significant increase in liver ALOX12 expression following hepatic IR insult, similar to what was observed in mice and in human cohorts (**Supplementary Fig. 8e,f**). After ML355 administration (**Supplementary Fig. 8g**), the serum concentration of ML355 reached its highest level as early as the ischemic stage and then gradually declined during the reperfusion stage, with a secondary increase at 12 h after reperfusion due to ML355 supplementation (**Supplementary Fig. 8h**). Notably, inhibiting 12-HETE production with ML355 significantly blocked IR-induced liver dysfunction and cell death, suppressed the production and release of cytokines and chemokines, and largely inhibited the activation of inflammatory signaling pathways (**Fig. 6c–e** and **Supplementary Fig. 8i–l**). Moreover, we performed perfusion CT examination and found systematic and long-term protection by ML355 against hepatic IR-induced liver injury (**Fig. 6f**). However, no significant effect of ML355 was observed in the setting of myocardial infarction (MI) or stroke (**Fig. 6g,h** and **Supplementary Fig. 9**), suggesting that the protective effect of blocking 12-HETE might be specific to hepatic IR injury among ischemia in different organs or to IR-related pathologies.

DISCUSSION

Hepatic IR can lead to severe liver injury and is a major cause for the failure of liver transplant surgery. Preventing and attenuating IR injury is an unmet clinical need²⁷. The current paradigm of hepatic IR is based on two apparently separate events, involving cell damage in the ischemic phase and inflammation during the reperfusion phase^{28,29}. It is also believed that ischemic insult can be readily tolerated by the liver, whereas the reperfusion-induced inflammatory response is the main culprit in liver destruction³⁰. Thus, recent efforts for therapeutic development have been focused on directly inhibiting inflammation and cell death at the reperfusion stage^{31,32}. However, therapeutic effects in rodent models have been limited, and the clinical benefits of this approach are uncertain. Here, using an unbiased systemic investigation based on an integrative omics approach and functional demonstration across multiple species ranging from mice to nonhuman primates, we have uncovered specific, robust and early reprogramming of lipid metabolism in the liver and notably in the AA pathway during the ischemic phase. It has been reported previously that the metabolic derangement of lipid profiles can induce inflammation, oxidative stress and apoptosis by regulating relevant signaling transduction pathways, which in turn can exacerbate lipid metabolic reprogramming^{33,34}. These findings support our results here and our conclusion that the pathogenesis of hepatic IR injury is marked primarily by lipid metabolic reprogramming that leads to a second-

ary effect on inflammation. Consequently, targeting the lipid profile reprogramming at the beginning of the ischemic stage can directly and effectively cut off the source of uncontrollable inflammation during the reperfusion stage to avoid subsequent cell death and liver damage. This insight not only provides a previously unknown cellular mechanism suggesting that ischemia is a necessary precursor for reperfusion-induced inflammation, but might also serve as the basis for a molecular mechanism of targeted therapeutic intervention.

The early changes in metabolism during the ischemic stage involve ALOX12 induction in hepatocytes and accumulation in the ischemic liver of 12-HETE, which acts as a key initiator of the subsequent inflammation and liver injury during reperfusion. A previous report identified succinate accumulation during ischemia as a critical metabolic change for induction of mitochondrial reactive oxygen species (ROS) during reperfusion³⁵, highlighting the importance of metabolism in the pathogenesis of IR injury. However, in contrast to the transient accumulation of succinate during the ischemic stage to promote oxidative stress, the dramatic change in the ALOX12–12-HETE axis is sustained throughout the entire process of IR and serves as a key driver of the inflammatory response. Furthermore, unlike succinate accumulation, which is a common ischemic signature, the function of 12-HETE appears to be tissue specific; therefore, 12-HETE is specifically effective as a therapeutic target in hepatic IR injury and not in heart (MI) or brain (stroke). The beneficial effects produced by inhibiting ALOX12–12-HETE induction in a mouse model of liver IR injury were conserved across large animals, including pigs and macaques, adding to the importance of this finding for potential clinical translation. Furthermore, considering that the dramatic accumulation of 12-HETE during the ischemic stage initiates hepatic IR injury, blocking the ALOX12–12-HETE axis during the early stage of ischemia is likely preferred to targeting a pathway in the later reperfusion stage. Although not explored here, the upregulated ALOX12 expression and increased 12-HETE content might act as crucial biomarkers in evaluation of liver injury and for prognosis after liver transplantation or resection.

The GPCR member GPR31 directly recognizes 12-HETE and mediates its function during the hepatic IR process. Since GPR31 was discovered as a 12-HETE receptor, its functional role has received very limited attention, with only a few recent reports regarding its potential role in cancer progression and KRAS activation^{36,37}. The potential participation of the GPCR superfamily in hepatic IR is largely unknown. Here we found that, during the hepatic IR process, upregulation of 12-HETE occurs and 12-HETE acts as a ligand for GPR31, activating downstream NF-κB and MAPK cascades to promote the production of proinflammatory cytokines and chemokines, as well as the subsequent leukocyte recruitment and activation^{22,38,39}. This excessive inflammation induces a massive loss of hepatocytes that exacerbates the severity of liver injury²⁸. We believe that this observation is translationally promising. The human genome encodes more than 800 GPCR family members⁴⁰. Notably, approximately 20–30% of US Food and Drug Administration (FDA)-approved drugs are targeted to GPCRs because of their relatively extensive pathological relevance and distribution in almost all cell types^{41,42}. Furthermore, the fact that GPCRs possess molecular pockets for small-molecule binding increases their drugability^{43,44}. Thus, GPR31 is a potential drug target in its own right. Furthermore, as 12-HETE–GPR31 signaling promotes a potent inflammatory response, targeting this axis may not only benefit therapy for hepatic IR injury but also that for other liver inflammatory diseases. In conclusion, our data delineate an ALOX12–12-HETE–GPR31 pathway as a key metabolic signaling axis in the pathogenesis of IR injury in the liver while calling for the development of more specific and effective

ALOX12 and/or GPR31 inhibitors that could potentially be used in therapy for hepatic IR injury.

METHODS

Methods, including statements of data availability and any associated accession codes and references, are available in the [online version of the paper](#).

Note: Any Supplementary Information and Source Data files are available in the online version of the paper.

ACKNOWLEDGMENTS

We thank Shanghai Metabolome Institute–Wuhan for their help in examining AA metabolites in the liver, serum and cell lysates. This work was supported by grants from the National Science Fund for Distinguished Young Scholars (no. 81425005; H.L.), the Key Project of the National Natural Science Foundation (no. 81330005 and 81630011; H.L.), the National Science and Technology Support Project (no. 2014BAI02B01 and 2015BAI08B01; H.L.), the National Key Research and Development Program (no. 2013YQ030923-05 (H.L.) and 2016YFF0101504 (Z.-G.S.)), the National Natural Science Foundation of China (no. 81770053; Z.-G.S.) and the Key Collaborative Project of the National Natural Science Foundation (no. 91639304; H.L. and Z.-G.S.).

AUTHOR CONTRIBUTIONS

X.-J.Z., X.C., Z.-Z.Y. and J.F. designed and performed the experiments, analyzed the data and wrote the manuscript; X.W. performed animal experiments, analyzed data and edited the manuscript; W.W. and Z.-Y.L. performed biological experiments and analyzed data; L.-J.S. analyzed data and organized figures; P.Z., P.-X.W. and Y.-X.J. performed omics analyses and provided important advice for this study; R.L. performed perfusion CT experiments; J.-Y.W. performed ultra-high-performance liquid chromatography–mass spectrometry experiments; S.T. established the animal hepatic IR models; X.-Y.Z. performed western blot experiments; Y.Z. performed staining experiments; R.-F.T. assisted in the performance of pig and monkey surgeries; L.W. collected clinical human liver and serum samples; X.-L.M., Z.H. and Z.-G.S. helped design the project and edited the manuscript; and H.L. designed experiments, wrote the manuscript and supervised the study.

COMPETING FINANCIAL INTERESTS

The authors declare no competing financial interests.

Reprints and permissions information is available online at <http://www.nature.com/reprints/index.html>. Publisher's note: Springer Nature remains neutral with regard to jurisdictional claims in published maps and institutional affiliations.

- Zhai, Y., Petrowsky, H., Hong, J.C., Busuttil, R.W. & Kupiec-Weglinski, J.W. Ischaemia–reperfusion injury in liver transplantation—from bench to bedside. *Nat. Rev. Gastroenterol. Hepatol.* **10**, 79–89 (2013).
- Vollmar, B. & Menger, M.D. The hepatic microcirculation: mechanistic contributions and therapeutic targets in liver injury and repair. *Physiol. Rev.* **89**, 1269–1339 (2009).
- Uchida, Y. *et al.* T-cell immunoglobulin mucin-3 determines severity of liver ischemia/reperfusion injury in mice in a TLR4-dependent manner. *Gastroenterology* **139**, 2195–2206 (2010).
- Wang, J.H. *et al.* Autophagy suppresses age-dependent ischemia and reperfusion injury in livers of mice. *Gastroenterology* **141**, 2188–2199 (2011).
- Clavien, P.A. *et al.* A prospective randomized study in 100 consecutive patients undergoing major liver resection with versus without ischemic preconditioning. *Ann. Surg.* **238**, 843–850, discussion 851–852 (2003).
- Eltzschig, H.K. & Eckle, T. Ischemia and reperfusion—from mechanism to translation. *Nat. Med.* **17**, 1391–1401 (2011).
- Zhai, Y., Busuttil, R.W. & Kupiec-Weglinski, J.W. Liver ischemia and reperfusion injury: new insights into mechanisms of innate-adaptive immune-mediated tissue inflammation. *Am. J. Transplant.* **11**, 1563–1569 (2011).
- Peralta, C., Jiménez-Castro, M.B. & Gracia-Sancho, J. Hepatic ischemia and reperfusion injury: effects on the liver sinusoidal milieu. *J. Hepatol.* **59**, 1094–1106 (2013).
- Mashima, R. & Okuyama, T. The role of lipoxygenases in pathophysiology: new insights and future perspectives. *Redox Biol.* **6**, 297–310 (2015).
- Tourdot, B.E. & Holinstat, M. Targeting 12-lipoxygenase as a potential novel antiplatelet therapy. *Trends Pharmacol. Sci.* **38**, 1006–1015 (2017).
- Powell, W.S. & Rokach, J. Biosynthesis, biological effects, and receptors of hydroxyeicosatetraenoic acids (HETEs) and oxoeicosatetraenoic acids (oxo-ETEs) derived from arachidonic acid. *Biochim. Biophys. Acta* **1851**, 340–355 (2015).
- Un, K. *et al.* Efficient suppression of murine intracellular adhesion molecule-1 using ultrasound-responsive and mannose-modified lipoplexes inhibits acute hepatic inflammation. *Hepatology* **56**, 259–269 (2012).
- Moles, A. *et al.* A TLR2/S100A9/CXCL-2 signaling network is necessary for neutrophil recruitment in acute and chronic liver injury in the mouse. *J. Hepatol.* **60**, 782–791 (2014).
- Tang, K. *et al.* Convergence of eicosanoid and integrin biology: 12-lipoxygenase seeks a partner. *Mol. Cancer* **14**, 111 (2015).
- Porro, B., Songia, P., Squellero, I., Tremoli, E. & Cavalca, V. Analysis, physiological and clinical significance of 12-HETE: a neglected platelet-derived 12-lipoxygenase product. *J. Chromatogr. B Analyt. Technol. Biomed. Life Sci.* **964**, 26–40 (2014).
- Johnson, E.N., Brass, L.F. & Funk, C.D. Increased platelet sensitivity to ADP in mice lacking platelet-type 12-lipoxygenase. *Proc. Natl. Acad. Sci. USA* **95**, 3100–3105 (1998).
- Luci, D.K. *et al.* Synthesis and structure–activity relationship studies of 4-((2-hydroxy-3-methoxybenzyl)amino)benzenesulfonamide derivatives as potent and selective inhibitors of 12-lipoxygenase. *J. Med. Chem.* **57**, 495–506 (2014).
- Husted, A.S., Traeulsen, M., Rudenko, O., Hjorth, S.A. & Schwartz, T.W. GPCR-mediated signaling of metabolites. *Cell Metab.* **25**, 777–796 (2017).
- Milligan, G., Alvarez-Curto, E., Hudson, B.D., Prihandoko, R. & Tobin, A.B. FFA4/GPR120: pharmacology and therapeutic opportunities. *Trends Pharmacol. Sci.* **38**, 809–821 (2017).
- Lu, J. *et al.* Structural basis for the cooperative allosteric activation of the free fatty acid receptor GPR40. *Nat. Struct. Mol. Biol.* **24**, 570–577 (2017).
- Im, D.S. FFA4 (GPR120) as a fatty acid sensor involved in appetite control, insulin sensitivity and inflammation regulation. *Mol. Aspects Med.* **S0098-2997(17)30064-X** (2017).
- Guo, Y. *et al.* Identification of the orphan G protein-coupled receptor GPR31 as a receptor for 12-(S)-hydroxyeicosatetraenoic acid. *J. Biol. Chem.* **286**, 33832–33840 (2011).
- Garcia, V. *et al.* 20-HETE signals through G-protein-coupled receptor GPR75 (Gq) to affect vascular function and trigger hypertension. *Circ. Res.* **120**, 1776–1788 (2017).
- Luci, D. *et al.* Discovery of ML355, a potent and selective inhibitor of human 12-lipoxygenase. In *Probe Reports from the NIH Molecular Libraries Program* (National Institutes of Health, 2010).
- Gregus, A.M. *et al.* Systematic analysis of rat 12/15-lipoxygenase enzymes reveals critical role for spinal eLOX3 hepxolin synthase activity in inflammatory hyperalgesia. *FASEB J.* **27**, 1939–1949 (2013).
- Cooper, D.K., Gollackner, B. & Sachs, D.H. Will the pig solve the transplantation backlog? *Annu. Rev. Med.* **53**, 133–147 (2002).
- Robertson, F.P., Fuller, B.J. & Davidson, B.R. An evaluation of ischaemic preconditioning as a method of reducing ischaemia/reperfusion injury in liver surgery and transplantation. *J. Clin. Med.* **6**, E69 (2017).
- Brenner, C., Galluzzi, L., Kepp, O. & Kroemer, G. Decoding cell death signals in liver inflammation. *J. Hepatol.* **59**, 583–594 (2013).
- Ju, C., Colgan, S.P. & Eltzschig, H.K. Hypoxia-inducible factors as molecular targets for liver diseases. *J. Mol. Med. (Berl.)* **94**, 613–627 (2016).
- van Golen, R.F., van Gulik, T.M. & Heger, M. The sterile immune response during hepatic ischemia/reperfusion. *Cytokine Growth Factor Rev.* **23**, 69–84 (2012).
- Datta, G., Fuller, B.J. & Davidson, B.R. Molecular mechanisms of liver ischemia reperfusion injury: insights from transgenic knockout models. *World J. Gastroenterol.* **19**, 1683–1698 (2013).
- Selznick, N., Rudiger, H., Graf, R. & Clavien, P.A. Protective strategies against ischemic injury of the liver. *Gastroenterology* **125**, 917–936 (2003).
- Corcoran, S.E. & O'Neill, L.A. HIF1α and metabolic reprogramming in inflammation. *J. Clin. Invest.* **126**, 3699–3707 (2016).
- Shimano, H. & Sato, R. SREBP-regulated lipid metabolism: convergent physiology — divergent pathophysiology. *Nat. Rev. Endocrinol.* <http://dx.doi.org/10.1038/nrendo.2017.91> (2017).
- Chouchani, E.T. *et al.* Ischaemic accumulation of succinate controls reperfusion injury through mitochondrial ROS. *Nature* **515**, 431–435 (2014).
- Fehrenbacher, N. *et al.* The G protein-coupled receptor GPR31 promotes membrane association of KRAS. *J. Cell Biol.* **216**, 2329–2338 (2017).
- Honn, K.V. *et al.* 12-HETE1/GPR31, a high-affinity 12(S)-hydroxyeicosatetraenoic acid receptor, is significantly up-regulated in prostate cancer and plays a critical role in prostate cancer progression. *FASEB J.* **30**, 2360–2369 (2016).
- Zhang, Q., Lenardo, M.J. & Baltimore, D. 30 years of NF-κB: a blossoming of relevance to human pathobiology. *Cell* **168**, 37–57 (2017).
- King, L.A., Toledo, A.H., Rivera-Chavez, F.A. & Toledo-Pereyra, L.H. Role of p38 and JNK in liver ischemia and reperfusion. *J. Hepatobiliary Pancreat. Surg.* **16**, 763–770 (2009).
- Stevens, R.C. *et al.* The GPCR Network: a large-scale collaboration to determine human GPCR structure and function. *Nat. Rev. Drug Discov.* **12**, 25–34 (2013).
- Wacker, D., Stevens, R.C. & Roth, B.L. How ligands illuminate GPCR molecular pharmacology. *Cell* **170**, 414–427 (2017).
- Rask-Andersen, M., Almén, M.S. & Schiöth, H.B. Trends in the exploitation of novel drug targets. *Nat. Rev. Drug Discov.* **10**, 579–590 (2011).
- Strasser, A., Wittmann, H.J. & Seifert, R. Binding kinetics and pathways of ligands to GPCRs. *Trends Pharmacol. Sci.* **38**, 717–732 (2017).
- Xiang, J. *et al.* Successful strategies to determine high-resolution structures of GPCRs. *Trends Pharmacol. Sci.* **37**, 1055–1069 (2016).

ONLINE METHODS

Digital gene expression. For the DGE assay, single-end libraries (with an insert size of 150 bp) were sequenced using an Illumina HiSeq 4000 with a read length of 49 bp. Reads with Illumina adaptor sequences, more than 5% non-ATCG bases or half of the bases showing low sequencing quality scores were first filtered from the raw data, resulting in approximately 10 million clean reads. All clean reads were then mapped to reference mRNA sequences from UCSC mm10 using short oligonucleotide analysis package 2 (SOAP2) (version 2.21), allowing no more than two mismatches; the insert size ranged from 0 to 1,000 (ref. 45). Normalized gene expression values were calculated using the reads per kilobase per million mapped reads (RPKM) method⁴⁶. A Student's *t*-test algorithm was used to identify differentially expressed genes between the different sample groups, and *P* values were corrected using the Benjamini–Hochberg algorithm. Differentially expressed genes defined from the pairwise comparisons had to satisfy two selection criteria, including (i) a fold change larger than 2 and (ii) corresponding *P* values less than 0.05.

Protein preparation and mass spectrometry. The liver tissue samples from each stage of hepatic IR injury were labeled with six tandem mass tags (TMTs) and used to conduct liquid chromatography–tandem mass spectrometry (LC–MS/MS) experiments using the Thermo Fisher Scientific Q Exactive HF system. The raw data obtained from the proteomics analysis were searched against the UniProt mouse protein sequences using the Proteome Discoverer software (version 1.4). The main parameters used in the integrated Mascot server were as follows: precursor tolerance 20 p.p.m.; fragment tolerance 0.1 Da; trypsin digestion; 2 missed cleavages; fixed modification of lysines and peptide N termini with TMT 6-plex and of cysteines with carbamidomethylation; and variable modifications of methionine with oxidation and of N termini with acetyl. Unique peptides with a 1% peptide false discovery rate (FDR) were reserved for protein quantification.

Clustering analysis. A hierarchical clustering analysis was performed to construct a phylogenetic tree of samples using an unweighted average distance (unweighted pair group method with arithmetic mean, UPGMA) algorithm. The R package ‘Rtsne’ was also employed to better visualize the profile of the gene expression data in 1D and 2D maps. *k*-means clustering was applied to explore the stage-specific gene expression patterns. The average gene expression levels of biological replicates were normalized using the Z-score transformation method and then imported into the multiple experiment viewer (MeV) 4.9 package, yielding six *k*-mean clusters with specific expression profiles. The enriched KEGG pathways in specific *k*-means clusters were then identified.

Kyoto Encyclopedia of Genes and Genomes pathway and gene set enrichment analyses. The annotation information regarding genes involved in biological pathways was obtained from the KEGG database. A KEGG pathway enrichment analysis was performed using Fisher's exact test with our in-house Perl script, and the annotation of all genes in the selected genome was used as the reference. Only pathways with a corresponding *P* value less than 0.05 were considered as significantly enriched. The hypergeometric Z-scores of these enrichments were calculated using the following formula

$$\text{hypergeometric Z-score} = \frac{m - (n \frac{M}{N})}{\sqrt{n \left(\frac{M}{N} \right) \left(1 - \frac{M}{N} \right) \left(1 - \frac{n-1}{N-1} \right)}}$$

where *N* and *n* are the number of all genes and the number of selected genes with KEGG annotation, respectively, and *M* and *m* are the number of all genes and the number of the same selected genes assigned to a given pathway.

Each known KEGG pathway or specific integrated gene list was defined as a gene set, and GSEA was implemented on the Java GSEA (version 2.2.4) platform with the ‘Signal2Noise’ metric to generate a ranked list and a ‘gene set’ permutation type. Gene sets with nominal *P* values less than 0.05 and FDR values less than 0.25 were considered statistically significant, and the leading-edge subsets that contributed most to the gene set enrichment signal were selected for the subsequent GO analysis.

Integrative omics analysis and data visualization using Circos. A total of 5,067 genes detected by both the mRNA expression data (nonzero RPKM) and proteomics protein abundance data were assigned to KEGG pathways. For each pathway, the Pearson correlation coefficient was used to estimate the conservation of the distinct profiles between ischemia and sham groups at the mRNA and protein levels, and the fold change of the mRNA expression or protein abundance was applied to calculate the Pearson correlation coefficient using the function ‘cor.test’ in R. A circular layout showing the correlation coefficients and *P* values of the pathways was generated using Circos (version 0.69)⁴⁷.

RNA-seq library preparation, sequencing and analysis. Paired-end RNA-seq was conducted in hepatocytes using Illumina HiSeq 4000 with an insert size of 250 bp and a read length of 150 bp. After removing low-quality reads, clean reads from the primary cultured mouse hepatocytes and human liver cell line L02 were aligned to the mouse (mm10) and human (hg38) genomes, respectively, using HISAT2 (version 2.1.0)⁴⁸. SAMtools (version 1.4.1) was used to produce BAM files to store the alignments of the unique mapped reads⁴⁹. Finally, cufflinks (version 2.2.1) was applied to estimate the FPKM value for each detected gene. The DGE and RNA-seq analyses were performed at the Beijing Genomics Institute (BGI).

Weighted gene coexpression network construction. The gene coexpression network was constructed using WGCNA (version 1.51)⁵⁰. All available biological replicates were averaged as WGCNA input. A soft power threshold of 22 was selected to ensure the network satisfied a scale-free topology ($R^2 > 0.90$) on the basis of the linear regression model fitting index obtained from the functions ‘pickSoftThreshold’ operation. Coexpression modules were detected using the function ‘blockwiseModules’ with the default settings and modified parameters (power, 22; minModuleSize, 30; mergeCutHeight, 0.25). Based on each module eigengene, a correlation analysis was performed to identify modules that were significantly associated with the measured traits.

Correlations between leading genes and 12-HETE function in hepatic injury were evaluated with a GO analysis performed on the basis of the coexpression network edge weights of highlighted leading-edge genes from the RNA-seq analysis following 12-HETE treatment under normoxia and hypoxia conditions (Fig. 5a). A heavier edge weight indicates a closer relationship between gene expression and biological function. After integrating the neighboring genes and edges (those with edge weight > 0.02) of the leading genes in the constructed coexpression network, edges were sorted according to weight and were assigned to corresponding biological process terms. An enrichment analysis was performed to determine whether the most connected neighbors (those in the heaviest 5% of edge weights) contributed to the indicated biological processes.

Animals and treatment. All animal protocols used in this study were approved by the Animal Care and Use Committee of Renmin Hospital of Wuhan University and the Institutional Animal Care and Use Committee of the Institute of Model Animals of Wuhan University. Animals received humane care according to the Guide for the Care and Use of Laboratory Animals published by the National Academy of Sciences and the National Institutes of Health. Abuse and maltreatment were avoided in our study.

Generation of genetically modified mice. To generate mice with a global knock-out allele for *Alox12* (*Alox12*-KO), a *Streptococcus pyogenes* Cas9 (SpCas9) target site in the conserved exon 5 was selected, and two single-strand oligonucleotide (ssOligonucleotide) primers were annealed and cloned into pUC57 vectors. The mRNA encoding the Cas9 nuclease and the short guide RNA (sgRNA) targeting *Alox12* were injected into zygotes from a C57BL/6 background. The genotypes of the generated mice were identified and confirmed by PCR assay using total DNA isolated from tails. The primers *Alox12*-P1 and *Alox12*-P2 were used to identify the deletion product. The *Gpr31b*-KO mice were generated using procedures similar to those used to generate the *Alox12*-KO mice, and the two specific target sites shown in Supplementary Table 1 were chosen because of the presence of multiple highly homologous transposons. The primers *Gpr31b*-P1 and *Gpr31b*-P2 were used to verify the deletion in the *Gpr31b* gene.

Alox12-HTG mice were generated using homologous recombination, and the full-length coding sequence of *Alox12* was cloned into an albumin vector under the control of a hepatocyte-specific promoter. The obtained plasmid was linearized and injected into zygotes. A PCR assay and sequencing were performed to confirm the genotype of mice. The primers used to identify the *Alox12* insertion were Alb-seq-F and Alb-seq-R. The primers and target sites used for mouse generation are listed in **Supplementary Table 1**.

Mouse hepatic ischemia–reperfusion model. Male mice aged 8–10 weeks (weight, 24–27 g) were subjected to 70% warm hepatic IR injury as previously described^{51,52}. Briefly, after the mice were anesthetized, midline laparotomy was performed to expose the liver. The blood supply to the left and median lobes was then occluded using an atraumatic microvascular clamp (Fine Science Tools, North Vancouver, BC, Canada). A successful ischemia operation was indicated by bleaching of the ischemic liver lobes. After 60 min of ischemia, the clamp was removed for reperfusion. At each indicated time point after reperfusion, mice were euthanized to collect liver samples and serum for subsequent examination. Mice that underwent the same surgical procedure without vasculature occlusion served as sham controls. Mice were maintained in a standard specific-pathogen-free environment (20–26 °C, 12-h light and 12-h dark cycle) with *ad libitum* access to food and water. ML355 (HY-12341; MCE, Monmouth Junction, NJ, USA) or CDC (ab141560; Abcam, Cambridge, MA, USA) in solution (DMSO: Solutol:PEG400:water; 5:10:20:65) was injected into mice via the tail vein at 30 min before ischemia and at 6 h after reperfusion at a dose of 3 mg per kg body weight. A blank solution was used as the vehicle control.

Human samples. The human serum and liver samples used in this study were obtained from patients who underwent liver resection surgery owing to hepatocellular carcinoma or hepatic cysts. Liver samples were collected from tumor- and cyst-free liver tissue from the individuals at three time points: before ischemia (baseline group), after ischemia but before reperfusion (ischemia group) and after reperfusion (reperfusion group). The serum samples were obtained at the same time points as the liver samples. Informed consent forms were signed by all donors or their families. All samples were used only to achieve the experimental objective, and the studies were performed according to the principles outlined by the Declaration of Helsinki. All procedures involving human samples were approved by the Renmin Hospital of Wuhan University Review Board and the Xijing Hospital of the Fourth Military Medical University Review Board. Clinical information regarding these individuals is provided in **Supplementary Table 2**.

qPCR assay. For the qPCR assay, total mRNA was extracted from liver tissue samples or cultured cells using TriPure Isolation Reagent (catalog no. 11667165001; Roche, Indianapolis, IN, USA). The isolated RNA was quantified and checked for quality using a Nanodrop 2000 (Thermo Fisher Scientific, Madison, WI, USA) and gel electrophoresis. 2 µg RNA was reverse-transcribed into cDNA using the Transcriptor First Strand cDNA Synthesis Kit (catalog no. 4896866001; Roche) following the manufacturer's instructions. The PCR amplification products were quantified by LightCycler 480 SYBR Green 1 Master Mix (catalog no. 04887352001; Roche) following a standard procedure (95 °C for 10 s, 60 °C for 10 s and 72 °C for 20 s; 45 cycles). The mRNA expression levels of the target genes were normalized to those of ACTB or 18S rRNA. The primer pairs used in this study are listed in **Supplementary Table 3**.

Western blot analysis and antibodies. Western blot analyses were performed as previously described⁵³. In brief, total protein was isolated from tissue or cell samples using RIPA lysis buffer (50 mM Tris-HCl, pH 7.4, 150 mM NaCl, 1% NP-40, 0.5% sodium deoxycholate, 0.1% SDS, 1 mM EDTA) with protease inhibitor cocktail tablets (catalog no. 04693132001; Roche) and phosphatase inhibitor tablets (catalog no. 4906837001; Roche) and quantified using a Pierce BCA Protein Assay Kit (catalog no. 23225; Thermo Fisher Scientific). The total protein samples were loaded and separated on SDS-PAGE gels and transferred to PVDF membranes (IPVH00010; Merck Millipore, Darmstadt, Germany). The membranes were blocked with 5% skim milk and incubated with the indicated primary antibodies overnight at 4 °C, which was followed by incubation with the corresponding secondary antibodies for 1 h at room temperature. Signals

were visualized by enhanced chemiluminescence (ECL) reagents (170-5061; Bio-Rad, Hercules, CA, USA) and captured by a ChemiDoc MP Imaging System (Bio-Rad). GAPDH was used as a loading control. Uncropped blots for western blots are shown in **Supplementary Figures 10–22**.

All antibodies used were purchased from and validated by commercial manufacturers. Antibodies against the following proteins were purchased from Cell Signaling Technology (Beverly, MA, USA): p-IκBα (catalog no. 9246), IκBα (catalog no. 4814), p-p65 (catalog no. 3033), p65 (catalog no. 4764), p-p38 (catalog no. 4511), p38 (catalog no. 9212), p-ERK1–ERK2 (catalog no. 4370), ERK1–ERK2 (catalog no. 4695), p-JNK1–JNK2 (catalog no. 4668), JNK1–JNK2 (catalog no. 9252), BCL2 (catalog no. 3498), BAX (catalog no. 2772), c-CASP3 (catalog no. 9664), p-PKC (catalog no. 2055), PKC (catalog no. 2058), ALOX5 (catalog no. 3289), CPLA2 (catalog no. 2832) and GAPDH (catalog no. 2118). Antibodies against ALOX12 were obtained from Santa Cruz (sc-365194, 1:200; Dallas, TX, USA) and Sigma (SAB2100109; St. Louis, MO, USA). Antibody against ALOX15 (sc-133085) was purchased from Santa Cruz Biotechnology. Antibodies against GPR31 (ab75579), GPR40 (ab211049), GPR75 (ab75581) and CYP4A (ab3573) were obtained from Abcam. Antibodies against GPR120 (sc-390752) were obtained from Santa Cruz Biotechnology. Secondary antibodies used in this study included Peroxidase AffiniPure goat anti-rabbit-IgG (H+L) (catalog no. 111-035-003) and goat anti-mouse-IgG (H+L) (catalog no. 115-035-003), which were purchased from the Jackson Laboratory (Bar Harbor, ME, USA). The Flag antibody was obtained from MBL (catalog no. M185-3L; Nagoya, Japan). Unless specified, all primary antibodies were used at the dilution of 1:1,000, and secondary antibodies were used at a 1:5,000 dilution.

Histological and immunohistochemical staining. H&E and immunohistochemical staining were performed in paraffin-embedded liver or heart sections. The waxes were sectioned serially at 5-µm thickness. After deparaffinization and rehydration, standard H&E staining was carried out to visualize the pattern in necrotic areas of the liver or heart. The TTC staining was performed as previously described⁵⁴ on brain sections (1 mm thick) to visualize the infarct volume of mice subjected to the cerebral IR procedure. The ALOX12 expression profile in mice and human liver samples was determined by incubating the liver sections with mouse anti-human-ALOX12 (sc-365194, 1:50 dilution; Santa Cruz) and rabbit anti-human ALOX12 (SAB2100109, 1:50 dilution; Sigma) primary antibodies, respectively. The infiltration of inflammatory cells into the liver sections of pigs was quantified using primary antibodies against CD11b (ab75476; Abcam), CD68 (MCA1957; AbD Serotec, Raleigh, NC, USA) and LY6G (catalog no. 551459, 1:25 dilution; BD Biosciences, San Jose, CA, USA). After overnight incubation with the primary antibodies at 4 °C, the sections were incubated with HRP-conjugated secondary antibodies (A21020, 1:500 dilution; Abbkine, Wuhan, China) and immunoreactive cells were visualized using DAB (ZLI-9032; Zhongshan Biotech, Beijing, China). The histological images were observed and captured under a light microscope (Olympus, Tokyo, Japan).

Sample preparation for UPLC–MS analysis. The content of AA metabolites in liver, serum and cell lysates, as well as the ML355 concentration in serum, was examined using ultra-high-performance liquid chromatography–mass spectrometry (UPLC–MS; 1290–6470 UHPLC–MS/MS system) as previously described^{55–57}. For liver samples, 50 mg of liver tissue was added to a polypropylene extraction tube and homogenized in 600 µl methanol containing 6 µl BHT (0.10 mM). The supernatant was further extracted with a 15% methanol aqueous solution and dried under nitrogen gas (N₂) using a Termovap Sample Concentrator. For serum samples, 150 µl cold methanol was added to 50 µl serum, vortexed for 30 s and centrifuged at 12,000g at 4 °C for 10 min. Supernatant was collected and dried under N₂ gas. For cultured cell samples, the cells were collected, counted and freeze-thawed three times in 600 µl of methanol. HETEs were extracted by sonication on ice. After centrifuging at 12,000g for 10 min, the separated supernatant was collected and dried following the procedure for liver and serum sample preparation. Samples were stored at –80 °C until analyses.

For the UPLC–MS examination, samples were dissolved in pure acetonitrile. An Agilent ZORBAX Eclipse Plus column (2.1 × 100 mm, 1.8 µm) was used for small molecule examination, and the column temperature was maintained at 45 °C. Metabolites were isolated using a biphasic system with a mobile phase A of 0.005% formic acid in water and a mobile phase B of 0.005% formic acid in

acetonitrile. The injection volume was 3 μ l, and the running rate was 0.6 ml per min. Small molecules were detected in negative multiple-reaction monitoring mode. The ionization parameters were set as follows: capillary voltage 3.5 kV, desolvation temperature 300 °C, desolvation gas flow rate 10 ml/h, nebulizer pressure 30 psi, sheath gas temperature 350 °C and sheath gas flow 11 l/min. Agilent MassHunter software (version B.08.00) was used for the quantitative analysis.

Cell lines and primary hepatocytes. HEK293T and L02 cells were purchased from the Type Culture Collection of the Chinese Academy of Sciences (Shanghai, China) and maintained in DMEM containing 10% FBS (catalog no. 10099141; Thermo Fisher Scientific), and 1% penicillin-streptomycin. No mycoplasma contamination was observed in the cells. No commonly misidentified cells were used in this study.

Primary hepatocytes were isolated from male mice aged 6–8 weeks using the collagenase perfusion method as described previously⁵⁸. Briefly, the liver was digested by administering a solution containing 0.5% collagenase type IV (catalog no. 17104-019; Thermo Fisher Scientific) through the portal vein. The liver was then excised, minced and filtered through a 70- μ m cell strainer (catalog no. 352350; Falcon, BD Biosciences). Primary hepatocytes were cultured in DMEM (catalog no. 11965-092; Invitrogen) supplemented with 10% FBS in plates coated with rat tail collagen at 37 °C in an incubator with 5% CO₂. The primary hepatocytes were challenged with hypoxia at an oxygen concentration of 1% for indicated periods, followed by reoxygenation to mimic *in vivo* hepatic IR injury. To examine the functional role of 12-HETE in hepatocytes, cells were treated with 12-HETE (34570; Cayman, Ann Arbor, MI, USA) at a dose of 100 nM. ML355 (10 μ M; HY-12341, MCE) was added to the cell medium to determine its inhibitory effects on 12-HETE production and function.

Plasmid construction. All plasmids used in this study were constructed following protocols described in previous studies⁵⁹. The full-length open reading frame (ORF) of the human gene *GPR31* was amplified from cDNA obtained by mRNA reverse transcription, and the sequences were cloned into the pcDNA5 vector. The knockdown plasmids for human *GPR31*, *GPR40*, *GPR75* and *GPR120* were constructed by inserting an shRNA targeting one of these genes into the pLKO.1 lentiviral vector. All plasmids were verified through sequencing. The primers used for plasmid construction are listed in **Supplementary Table 4**.

Lentivirus and adenovirus production and infection. To generate stably transfected cells with stable knockdown of *GPR31*, *GPR40*, *GPR75* or *GPR120* expression, we constructed lentiviral vectors as previously described⁵⁹. An shRNA targeting GFP was used as the control. For the lentivirus production, HEK293T cells were cotransfected with the constructed lentivirus and packaging plasmids psPAX2 and pMD2.G. The replication-defective virus was harvested and used to infect host cells with 10 μ g/ml polybrene. Cells stably expressing each construct were obtained after puromycin screening and verified by western blot analyses. The adenoviruses used to overexpress or interfere with mouse *Alox12* in the primary hepatocytes were purchased from Hanbio Biotechnology Co., Ltd. (Shanghai, China). All procedures involving virus operation were performed in a biosafety cabinet.

***GPR31*-knockout cell line generation.** The human *GPR31*-knockout cell line was constructed using a dual-vector SpCas9 system in L02 cells as previously described⁶⁰. sgRNA targeting human *GPR31* was cloned into the pGL3-U6-sgRNA-PGK-puromycin vector and cotransfected with the pST1374-N-NLS-Flag-Linker-Cas9 plasmid into human L02 hepatocytes. Homozygous *GPR31*-knockout cells were obtained from a monoclonal line after puromycin and blasticidin screening. The target site for human *GPR31* was 5'-TCCACACCTGACCGGAAC-3'. The sequencing primers are listed in **Supplementary Table 4**.

Liver function examination. The liver function of animals in this study was assayed by measuring the concentrations of ALT, AST and ALP in serum using an ADVIA 2400 Chemistry System analyzer (Siemens, Tarrytown, NY, USA) according to the manufacturer's instructions.

Heart function assay. The heart function of mice was evaluated by measuring serum concentrations of creatine kinase (CK) and lactate dehydrogenase (LDH) by ADVIA 2400 Chemistry System analyzer (Siemens) according to the manufacturer's instructions. Echocardiographic assay was also performed to examine heart function of mice after MI surgery using a MyLab 30CV ultrasound (Biosound Esaote Inc.) with a 15-MHz probe, as reported by previous studies^{61,62}.

Immunofluorescence and TUNEL staining. The liver sections used for the immunofluorescence and TUNEL staining assays were prepared through fixation in 4% neutral paraformaldehyde for more than 48 h, followed by embedding in paraffin. The thickness of the liver sections was 5 μ m. To examine the infiltration of inflammatory cells, mouse liver sections were first blocked with 10% goat serum and then incubated with rabbit anti-mouse-CD11b (ab75476, 1:100 dilution; Abcam) or rabbit anti-mouse-Ly6G (catalog no. 551459, 1:25 dilution; BD Biosciences) primary antibodies at 4 °C overnight. Goat anti-rabbit-IgG (A-11011, 1:200 dilution; Thermo Fisher Scientific) was applied as the secondary antibody. TUNEL staining was performed to evaluate liver injury using an ApopTag Plus *In Situ* Apoptosis Fluorescein Detection Kit (S7111; Millipore) according to the manufacturer's instructions. The nuclei were labeled with DAPI. Images were obtained under a fluorescence microscope (Olympus DX51).

Serum concentration of inflammatory mediators. The concentration of inflammatory cytokines and chemokines (tumor necrosis factor (TNF), IL-6, CCL2 and CXCL10) in serum were determined by ELISA (mouse: SEA133Mu 96T for TNF, SEA087Mu 96T for CCL2 and SEA371Mu 96T for CXCL10; pig: SEA079Po 96T for IL-6 and SEA087Po 96T for CCL2; monkey: SEA079Si 96T for IL-6 and SEA087Si 96T for CCL2). All commercial kits were purchased from Cloud-Clone Corp. (Wuhan, China) and used according to the manufacturer's instructions.

Pig hepatic ischemia–reperfusion model. Male domestic pigs (Wanqian Jiaxing, Wuhan, China) aged 3 months (weight, 18–30 kg) were used in this study. For the full hepatic IR surgery, pigs were first sedated with Shumianning II (0.15 ml per kg body weight; Nanjing Agricultural University, Nanjing, China), followed by administration of 0.02 mg per kg body weight atropine (Kelong, Ruicheng, Shandong, China). Anesthesia was maintained by inhaled isoflurane at 1.5–3% after atracurium intravascular injection (0.15 mg per kg body weight). Midline laparotomy was performed to expose the liver hilum. Total hepatic warm ischemia was achieved by simultaneously clamping the hepatic artery and the portal vein after heparinization. To avoid splanchnic congestion, the portal flow was bypassed to the right external jugular vein, and the pressure in the bypass cannula was kept below 20 cm H₂O. Microcirculatory perfusion was examined by a laser Doppler perfusion monitoring unit (PeriFlux System 5000; Perimed, Ardmore, PA, US) before and at 10 min after clamping, and a 70–80% reduction of microperfusion was considered adequate ischemia. After a 120-min period of ischemia, all cannulas were withdrawn and the clamps were released to restore the inflow to the liver. The abdominal wall was then closed, but the central vein catheter was not removed from the neck to allow blood collection and drug administration after the operation. After 48 h of reperfusion, pigs were euthanized and liver samples were collected for subsequent examination.

ML355 was administered at a dose of 0.4 mg per kg body weight (DMSO: Solutol:PEG400:water; 5:10:20:65) 30 min before ischemia through the portal vein, and the same dose was delivered via the internal jugular vein 6 h after reperfusion. The control pigs received an equal volume of vehicle solution. Surgery was performed under sterile conditions. The vital signs of pigs were recorded and are shown in **Supplementary Table 5**.

Monkey hepatic ischemia–reperfusion model. All rhesus monkeys used in this study were purchased from Hubei Topgene Laboratory Animal Science and Technology Co. Ltd. (Suizhou, China). Only male monkeys aged 4–6 years and weighing 4–6 kg were included. All monkeys were in good general health and passed the local quarantine test. Monkeys were acclimated to their housing facilities for at least 28 d before the operation. The monkeys were individually housed in standard primate cages, fed a special chow for nonhuman primates and seasonal fruits, and had free access to water. The room lighting was maintained

on a 12-h dark–12-h light automatic cycle, and the room temperature was maintained at 22–26 °C.

For the hepatic IR surgery, the monkeys were anesthetized with an intramuscular injection of 0.1 ml per kg body weight Shumianning II and 0.02 mg per kg body weight atropine, followed by an atracurium (0.15 mg per kg body weight) intravascular injection to induce muscle relaxation. Anesthesia was maintained by 1–1.5% inhaled isoflurane during the entire surgery process. Median laparotomy was then performed to expose the liver, and the ligament between the left lateral lobe and the median lobe was occluded using an atraumatic right-angle clamp after heparinization. Care was taken to prevent damaging the liver tissues before the clamp was tightened. After a period of warm ischemia (30, 60 or 120 min), the clamp was released to allow reperfusion. Ischemia and reperfusion were considered successful when the microperfusion was reduced to less than 20% during ischemia and restored with reperfusion. After reperfusion, the abdomen was closed. To evaluate the effect of ALOX12 inhibition on hepatic IR injury, ML355 (3 mg per kg body weight in a solution of DMSO:Solutol:PEG400:water; 5:10:20:65) was administered 30 min before blood blockage through the portal vein and at 6 h after reperfusion through the saphenous vein. Liver samples were collected from the left lateral and median lobes after 48 h of reperfusion. Postoperative pain was alleviated with 0.1 ml per kg body weight Tolfedine injected intramuscularly. Vital signs were monitored and are shown in **Supplementary Table 6**.

Perfusion computed tomography imaging. At 48 h, 1 week, 2 weeks, 3 weeks and 4 weeks after inducing hepatic IR injury, liver injury in the monkeys was evaluated using perfusion CT imaging using a Siemens SOMATOM Definition 64 (Siemens Medical Solutions USA, Inc.). At 30 min before CT scanning, the monkey was anesthetized and fixed on a scanning table in a supine position. An intravenous line was established and connected to the contrast material. After localization scans were acquired in two orthogonal directions, a noncontrast helical scan covering the entire abdomen was performed at 27 effective mAs and 100 kV (number of scans, 66; slice thickness, 5 mm; rotation time, 0.5 s; delay, 2 s). A perfusion CT examination was then performed using an iodixanol injection (catalog no. 92339-11-2; Jiang Su Heng Rui Medicine Co., Ltd., Lianyungang, China) as the contrast material at a dose of 2 ml per kg body weight, followed by a 15-ml saline flush at a rate of 2 ml/s. The perfusion scan began when the contrast solution was intravenously injected and was followed by ten noncontrast scans. A total of 39 scans at a scan interval of 3 s were performed. The perfusion CT data were collected and transferred to the Philips IntelliSpace Portal workstation (version 06.0.3.12200), and perfusion maps of hepatic arterial perfusion, hepatic portal perfusion, total liver perfusion and the hepatic perfusion index were generated.

Mouse myocardial infarction model, stroke model and treatment. The mouse MI model was established by ligating the left coronary artery as previously reported⁶³. Briefly, mice were anesthetized using sodium pentobarbital (50 mg per kg body weight, intraperitoneally) and then subjected to a left thoracotomy at the third or fourth intercostal space. After the pericardium was opened, the proximal left coronary descending (LAD) artery was encircled and ligated using a 7-0 silk suture. Mice in the sham group underwent the same procedure without LAD ligation.

The mouse stroke model was established by transiently occluding the left middle cerebral artery according to previous studies⁶⁴. After mice were anesthetized by 2.5–3% isoflurane in oxygen, the left common, internal and external carotid arteries were exposed. A 6-0 silicon-coated monofilament was then inserted into the internal carotid artery and blocked the origin of the middle cerebral artery. After 45 min of ischemia, the filament was withdrawn to restore blood flow for the indicated period. The regional cerebral blood flow during surgery was monitored by Doppler analysis (Periflux System 5010; Perimed, Sweden).

Mice in the ML355 group were injected with ML355 in the tail vein at 3 mg per kg body weight per day for a continuous 7 d in the MI model. To evaluate the function of ML355 on stroke, mice were injected with ML355 at 3 mg per kg body weight at 30 min before surgery and after 6 h of reperfusion in the tail vein. A blank solution was injected as vehicle into control mice.

Statistical analysis. All statistical analyses used in this study were performed using SPSS (version 21.0), and the data are expressed as the mean ± s.e.m. unless

otherwise indicated. Statistical differences between two groups were calculated by two-tailed Student's *t*-test, and one-way ANOVA was performed for comparisons among more than two groups using a Bonferroni *post hoc* analysis if the data had a normal distribution and homogeneity of variance or using Tamhane's T2 (M) analysis when there was heteroscedasticity in the data. Pairwise comparisons were performed only when the global null hypothesis was rejected. The variance was similar among the compared groups. Statistical differences with *P* values less than 0.05 were considered significant. Detailed statistical information for each experiment is provided in the corresponding figure legends. The sample sizes for each set of animals were determined according to previous studies performed by our group and other scholars and were fixed in a prospective manner. One mouse in the *Alox12-HTG/rep* 6 h (at 6 h after reperfusion) group died before the sample collection and thus was excluded from statistical analysis. Animals with the same genotype and similar baseline values were randomly assigned to the sham and surgery groups or the vehicle and ML355 treatment groups. The experimenters were blinded to animal genotype and grouping information. All *in vitro* experiments were performed in triplicate unless specified in the figure legends.

Life Sciences Reporting Summary. Further information on experimental design is available in the **Life Sciences Reporting Summary**.

Data availability. The data sets supporting the conclusions of this article are included within the article and its additional files. The DGE and transcriptomics data have been submitted to the Sequence Read Archive with the database identifiers [SRP117594](#), [SRP117665](#) and [SRP117667](#). The mass spectrometry proteomics data have been deposited to the ProteomeXchange Consortium via the proteomics identification (PRIDE) partner repository with the data set identifier [PXD007827](#). Plasmids are available from the corresponding author upon reasonable request.

45. Li, R. *et al.* SOAP2: an improved ultrafast tool for short read alignment. *Bioinformatics* **25**, 1966–1967 (2009).
46. Mortazavi, A., Williams, B.A., McCue, K., Schaeffer, L. & Wold, B. Mapping and quantifying mammalian transcriptomes by RNA-Seq. *Nat. Methods* **5**, 621–628 (2008).
47. Krzywinski, M. *et al.* Circos: an information aesthetic for comparative genomics. *Genome Res.* **19**, 1639–1645 (2009).
48. Kim, D., Langmead, B. & Salzberg, S.L. HISAT: a fast spliced aligner with low memory requirements. *Nat. Methods* **12**, 357–360 (2015).
49. Li, H. *et al.* The Sequence Alignment/Map format and SAMtools. *Bioinformatics* **25**, 2078–2079 (2009).
50. Langfelder, P. & Horvath, S. WGCNA: an R package for weighted correlation network analysis. *BMC Bioinformatics* **9**, 559 (2008).
51. Wang, X. *et al.* Dusp14 protects against hepatic ischemia–reperfusion injury via Tak1 suppression. *J. Hepatol.* **S0168-8278(17)32275-4** (2017).
52. Hu, J. *et al.* Targeting TRAF3 signaling protects against hepatic ischemia/reperfusion injury. *J. Hepatol.* **64**, 146–159 (2016).
53. Sun, P. *et al.* Mindin deficiency protects the liver against ischemia/reperfusion injury. *J. Hepatol.* **63**, 1198–1211 (2015).
54. Li, L. *et al.* Attenuation of cerebral ischemic injury in interferon regulatory factor 3-deficient rat. *J. Neurochem.* <http://dx.doi.org/10.1111/jnc.13448> (2015).
55. Martin-Venegas, R., Jáuregui, O. & Moreno, J.J. Liquid chromatography–tandem mass spectrometry analysis of eicosanoids and related compounds in cell models. *J. Chromatogr. B Analys. Technol. Biomed. Life Sci.* **964**, 41–49 (2014).
56. Masoodi, M., Eiden, M., Koulman, A., Spaner, D. & Volmer, D.A. Comprehensive lipidomics analysis of bioactive lipids in complex regulatory networks. *Anal. Chem.* **82**, 8176–8185 (2010).
57. Zhu, Q.F. *et al.* Analysis of cytochrome P450 metabolites of arachidonic acid by stable isotope probe labeling coupled with ultra high-performance liquid chromatography/mass spectrometry. *J. Chromatogr. A* **1410**, 154–163 (2015).
58. Wang, P.X. *et al.* Targeting CASP8 and FADD-like apoptosis regulator ameliorates nonalcoholic steatohepatitis in mice and nonhuman primates. *Nat. Med.* **23**, 439–449 (2017).
59. Zhao, G.N. *et al.* Tmbim1 is a multivesicular body regulator that protects against non-alcoholic fatty liver disease in mice and monkeys by targeting the lysosomal degradation of Tlr4. *Nat. Med.* **23**, 742–752 (2017).
60. Shalem, O. *et al.* Genome-scale CRISPR–Cas9 knockout screening in human cells. *Science* **343**, 84–87 (2014).
61. Jiang, X. *et al.* Tumor necrosis factor receptor-associated factor 3 is a positive regulator of pathological cardiac hypertrophy. *Hypertension* **66**, 356–367 (2015).
62. Ji, Y.X. *et al.* The ubiquitin E3 ligase TRAF6 exacerbates pathological cardiac hypertrophy via TAK1-dependent signalling. *Nat. Commun.* **7**, 11267 (2016).
63. Bao, M.W. *et al.* Cardioprotective role of growth/differentiation factor 1 in post-infarction left ventricular remodelling and dysfunction. *J. Pathol.* **236**, 360–372 (2015).
64. Guo, S. *et al.* Oncostatin M confers neuroprotection against ischemic stroke. *J. Neurosci.* **35**, 12047–12062 (2015).

Life Sciences Reporting Summary

Nature Research wishes to improve the reproducibility of the work that we publish. This form is intended for publication with all accepted life science papers and provides structure for consistency and transparency in reporting. Every life science submission will use this form; some list items might not apply to an individual manuscript, but all fields must be completed for clarity.

For further information on the points included in this form, see [Reporting Life Sciences Research](#). For further information on Nature Research policies, including our [data availability policy](#), see [Authors & Referees](#) and the [Editorial Policy Checklist](#).

► Experimental design

1. Sample size

Describe how sample size was determined.

The sample sizes of each set of animals were determined according to previous studies performed by our group and other scholars and were fixed in a prospective manner.

2. Data exclusions

Describe any data exclusions.

One mouse in Alox12-HTG/Rep 6h group died before the sample collection and thus were excluded for statistical analysis

3. Replication

Describe whether the experimental findings were reliably reproduced.

All in vitro experiments were performed in triplicate unless specified in the figure legends. The detailed replication of each experiments has been provided in Figure Legend. All attempts at replication were successful for all experiments.

4. Randomization

Describe how samples/organisms/participants were allocated into experimental groups.

Animals with the same genotype and similar baseline values were randomly assigned to the sham and surgery groups or the vehicle and ML355 groups.

5. Blinding

Describe whether the investigators were blinded to group allocation during data collection and/or analysis.

The experimenters were blinded to the animal genotype and grouping information.

6. Statistical parameters

For all figures and tables that use statistical methods, confirm that the following items are present in relevant figure legends (or in the Methods section if additional space is needed).

n/a Confirmed

- The exact sample size (*n*) for each experimental group/condition, given as a discrete number and unit of measurement (animals, litters, cultures, etc.)
- A description of how samples were collected, noting whether measurements were taken from distinct samples or whether the same sample was measured repeatedly
- A statement indicating how many times each experiment was replicated
- The statistical test(s) used and whether they are one- or two-sided (note: only common tests should be described solely by name; more complex techniques should be described in the Methods section)
- A description of any assumptions or corrections, such as an adjustment for multiple comparisons
- The test results (e.g. *P* values) given as exact values whenever possible and with confidence intervals noted
- A clear description of statistics including central tendency (e.g. median, mean) and variation (e.g. standard deviation, interquartile range)
- Clearly defined error bars

See the web collection on [statistics for biologists](#) for further resources and guidance.

► Software

Policy information about [availability of computer code](#)

7. Software

Describe the software used to analyze the data in this study.

Agilent MassHunter software (version B.08.00) was used for the quantitative analysis of UPLC-MS.
Philips IntelliSpace Portal workstation (version 06.0.3.12200) was used to analyze the perfusion CT data.
All clean reads were mapped to reference sequences using SOAP2 (version 2.21) in DGE analysis.
Proteome Discoverer software (version 1.4) was used to search against the Uniport mouse protein sequences in proteomics analysis.
MeV (version 4.9) was used for K-means clustering analysis.
GSEA was implemented in the java GSEA (version 2.2.4).
A circular layout showing the correlation coefficients and P values of the pathways was generated using Circos (version 0.69).
Clean reads were aligned by HISAT2 (version 2.1.0) in RNA-seq analysis.
SAMtools (version 1.4.1) was used to produce BAM files in RNA-seq analysis.
Cufflinks (version 2.2.1) was applied to estimate the gene expression in RNA-seq analysis.
The gene co-expression network was constructed using WGCNA (version 1.51).
All statistical analyses used in this study were performed using SPSS (Version 21.0).

For manuscripts utilizing custom algorithms or software that are central to the paper but not yet described in the published literature, software must be made available to editors and reviewers upon request. We strongly encourage code deposition in a community repository (e.g. GitHub). [Nature Methods guidance for providing algorithms and software for publication](#) provides further information on this topic.

► Materials and reagents

Policy information about [availability of materials](#)

8. Materials availability

Indicate whether there are restrictions on availability of unique materials or if these materials are only available for distribution by a for-profit company.

Agilent MassHunter software was used for the quantitative analysis. The data sets supporting the conclusions of this article are included within the article and its additional files. The DGE and transcriptomics data have been submitted to NCBI Sequence Read Archive with the database identifier of SPR117594, SPR117665 and SPR117667. The mass spectrometry proteomics data have been deposited to the ProteomeXchange Consortium via the PRIDE partner repository with the dataset identifier PXD007827. Plasmids are available upon reasonable request. A Life Sciences Reporting Summary for this paper is available.

9. Antibodies

Describe the antibodies used and how they were validated for use in the system under study (i.e. assay and species).

The detailed information of all antibodies used in our present study has been provided in the "Western blot analysis and antibodies" section in ONLINE METHODS. Antibodies against the following proteins were purchased from Cell Signaling Technology (Beverly, Massachusetts, USA): p-Ikba (#9246), Ikba (#4814), p-p65 (#3033), p65 (#4764), p-p38 (#4511), p38 (#9212), p-ERK1–ERK2 (#4370), ERK1–ERK2 (#4695), p-JNK1–JNK2 (#4668), JNK1–JNK2 (#9252), BCL2 (#3498), BAX (#2772), c-caspase3 (#9664), p-PKC (#2055), PKC (#2058), ALOX5 (#3289), CPLA2 (#2832) and GAPDH (#2118). Antibodies against ALOX12 were obtained from Santa Cruz (sc-365194; 1:200; Dallas, TX, USA) and Sigma (SAB2100109; St.Louis, MO, USA). ALOX15 (sc-133085) antibody was purchased from Santa Cruz Biotechnology. Antibodies against GPR31 (ab75579), GPR40 (ab211049), GPR75 (ab75581) and CYP4A (ab3573) were obtained from Abcam. GPR120 (sc-390752) was obtained from Santa Cruz Biotechnology. Secondary antibodies used in this study included Peroxidase AffiniPure goat anti-rabbit-IgG (H+L) (#111-035-003) and goat anti-mouse-IgG (H+L) (#115-035-003), which were purchased from the Jackson Laboratory (Bar Harbar, ME, USA). The Flag antibody was obtained from medical and biological laboratories (MBL, Nagoya, Japan). Unless specified, all primary antibodies were used at the dilution of 1:1000, and secondary antibodies were used at a 1:5,000 dilution.

10. Eukaryotic cell lines

- a. State the source of each eukaryotic cell line used.
- b. Describe the method of cell line authentication used.
- c. Report whether the cell lines were tested for mycoplasma contamination.
- d. If any of the cell lines used are listed in the database of commonly misidentified cell lines maintained by ICLAC, provide a scientific rationale for their use.

The HEK293T and L02 cells were purchased from the Type Culture Collection of the Chinese Academy of Sciences (Shanghai, China).

The HEK293T and L02 cell lines were verified by short tandem-repeat DNA profiling before the study.

No mycoplasma contamination was observed in the cells.

No commonly misidentified cells were used in this study.

► Animals and human research participants

Policy information about [studies involving animals](#); when reporting animal research, follow the [ARRIVE guidelines](#)

11. Description of research animals

Provide details on animals and/or animal-derived materials used in the study.

The detailed information about animals and animal-derived materials used in this study has been provided in our ONLINE METHODS section.

Male mice aged 8-10 weeks (24-27 g) were subjected to a 70% warm hepatic IR injury. Mice were maintained in a standard SPF environment with ad libitum access to food and water. ML355 (HY-12341; MCE, Monmouth Junction, NJ, USA) or CDC (ab141560; Abcam, Cambridge, MA, USA) in the solution (DMSO : Solutol : PEG400 : water; 5/10/20/65 v/v/v/v) was injected into mice via the tail vein at 30 min before ischemia and at 6 h after reperfusion at a dose of 3 mg/kg. A blank solution was used as the vehicle control.

Primary hepatocytes were isolated from male mice aged 6-8 weeks using collagenase perfusion method.

All animal protocols used in this study were approved by the Animal Care and Use Committee of Renmin Hospital of Wuhan University and Institutional Animal Care and Use Committee of the Institute of Model Animal of Wuhan University. Animals received humane care according to Guide for the Care and Use of Laboratory Animals published by the National Academy of Sciences and the National Institutes of Health. Abuse and maltreatment were avoided in our study.

Policy information about [studies involving human research participants](#)

12. Description of human research participants

Describe the covariate-relevant population characteristics of the human research participants.

The descriptions of characteristics of human samples have been provided in the "Human samples" section and in Supplementary Table 2.

The human serum and liver samples used in this study were obtained from patients who underwent liver resection surgery due to hepatocellular carcinoma or hepatic cyst. Liver samples were collected from normal liver tissues of individuals at 3 time points, including before ischemia (baseline group), after ischemia but before reperfusion (ischemia group), and after reperfusion (reperfusion group). The serum samples were obtained at the same time points as the liver samples. Informed consent forms were signed by all donors or their families. All these samples were used only to achieve experimental objective, and the studies were performed according to the principles outlined by the Declaration of Helsinki. All procedures involving human samples were approved by the Renmin Hospital of Wuhan University Review Board and Xijing hospital of The Fourth Military Medical University Review Board.